

Globally resolved surface temperatures since the Last Glacial Maximum

<https://doi.org/10.1038/s41586-021-03984-4>

Received: 26 March 2021

Accepted: 1 September 2021

Published online: 10 November 2021

 Check for updates

Matthew B. Osman¹✉, Jessica E. Tierney¹, Jiang Zhu², Robert Tardif³, Gregory J. Hakim³, Jonathan King¹ & Christopher J. Poulsen⁴

Climate changes across the past 24,000 years provide key insights into Earth system responses to external forcing. Climate model simulations^{1,2} and proxy data^{3–8} have independently allowed for study of this crucial interval; however, they have at times yielded disparate conclusions. Here, we leverage both types of information using paleoclimate data assimilation^{9,10} to produce the first proxy-constrained, full-field reanalysis of surface temperature change spanning the Last Glacial Maximum to present at 200-year resolution. We demonstrate that temperature variability across the past 24 thousand years was linked to two primary climatic mechanisms: radiative forcing from ice sheets and greenhouse gases; and a superposition of changes in the ocean overturning circulation and seasonal insolation. In contrast with previous proxy-based reconstructions^{6,7} our results show that global mean temperature has slightly but steadily warmed, by ~0.5 °C, since the early Holocene (around 9 thousand years ago). When compared with recent temperature changes¹¹, our reanalysis indicates that both the rate and magnitude of modern warming are unusual relative to the changes of the past 24 thousand years.

The interval of time spanning the Last Glacial Maximum (LGM; 21–18 thousand years ago, ka) to the preindustrial era represents the most recent large-scale reorganization of the climate system, over which the Earth rapidly transitioned out of a cold, glaciated state with vast Northern Hemisphere ice sheets into a warm interglacial. Constraining the evolution of global surface temperatures during this critical time period provides an excellent opportunity to better understand the mechanisms of large-scale climate change, including Earth system interactions and responses to various forcings (for example, greenhouse gases, albedo/ice-sheet and orbital changes).

A number of prior studies have sought to characterize the global surface temperature evolution from the LGM to present^{3–7}. Of particular note, Shakun et al.³ and Marcott et al.⁶ established a global mean surface temperature (GMST) estimate spanning the deglacial and Holocene periods using ~80 marine and terrestrial temperature proxies (hereafter, the Shakun–Marcott curve; SMC). However, subsequent comparisons of SMC to other global temperature reconstructions and transient LGM-to-present model simulations revealed discrepancies surrounding the timing, magnitude, and rapidity of deglacial warming and of millennial-scale cooling events^{2,4}. One of the most prominent differences between SMC and climate model simulations is the direction of global temperature change across the Holocene. Whereas SMC shows a cooling trend, modelling results indicate there should be a warming, a phenomenon termed the Holocene temperature conundrum². More recent work has sought to reconcile these differences by using either independent^{12,13} or additional^{7,11} proxies, and by correcting for possible proxy seasonal biases^{2,8,12}. Nonetheless, all of these approaches have a fundamental limitation in that none provide a

dynamically constrained full-field view of climate evolution since the LGM. Conversely, although climate models provide a self-consistent and spatially complete representation of the climate system, they are known to have biases due to inaccurate representation of climate processes^{10,14}. Moreover, the fidelity of paleoclimate simulations of the LGM and Holocene depends on the accurate knowledge of paleoclimate boundary conditions, which are known with varying levels of certainty and may not be independent from proxies^{2,15,16}.

The Last Glacial Maximum reanalysis

Here, we revisit the evolution of global temperatures from the LGM to present using an offline paleoclimate data assimilation approach that formally combines proxy and independent model information^{9,10,17}. The resulting ‘Last Glacial Maximum reanalysis’ (LGMR) product offers the first proxy-constrained, dynamically consistent and spatiotemporally complete view of climate change for the past 24 kyr. The LGMR enables us to diagnose the major modes of climate variability, refine our understanding of global temperature changes across the Holocene, and compare current anthropogenic global warming with the rate and magnitude of change seen in the recent geological record.

Following ref.¹⁰, we focus on assimilating geochemical proxies for sea surface temperature (SST) with established Bayesian proxy forward models^{18–21}. To ensure that the proxy data have sufficient temporal resolution and length to inform our reconstruction, we required that records be at least 4,000 years long, have a median time resolution of 1,000 years or less, and contain a radiocarbon-based

¹Department of Geosciences, University of Arizona, Tucson, AZ, USA. ²Climate and Global Dynamics Laboratory, National Center for Atmospheric Research, Boulder, CO, USA. ³Department of Atmospheric Sciences, University of Washington, Seattle, WA, USA. ⁴Department of Earth and Environmental Sciences, University of Michigan, Ann Arbor, MI, USA. ✉e-mail: mattosman@arizona.edu

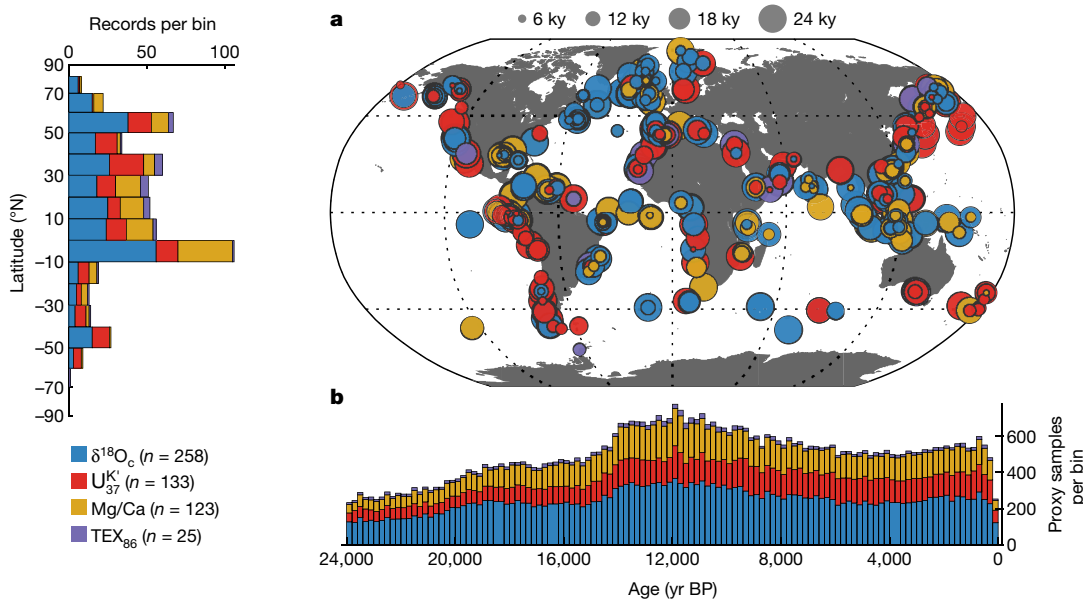


Fig. 1 | Locations and temporal coverage of the SST proxies. **a**, Site locations of TEX_{86} , Mg/Ca, U_{37}^K and $\delta^{18}\text{O}_c$ records (right), as well as their latitudinal distribution (left). Bubble diameter corresponds to temporal coverage of

each record. **b**, Temporal coverage of the proxies, binned at 200-year intervals. Years before present (yr BP) are relative to 1950 CE.

age model. The temporal criteria were relaxed for several (seven) sites in the Southern Ocean to increase coverage in this data-poor region. Conversely, some SST records that met these criteria were excluded due to complications related to proxy interpretation and (or) their location (Methods). In total, our vetted compilation consists of 539 records, including 133 alkenone (U_{37}^K), 25 TetraEther indeX of 86 carbons (TEX_{86}), 123 planktic foraminiferal Mg/Ca, and 258 planktic foraminiferal oxygen isotope ($\delta^{18}\text{O}_c$) time series (Fig. 1 and Extended Data Fig. 1).

The diversity, size and spatial coverage of our proxy compilation offers new insight into LGM-to-present climate evolution on its own. However, transient offline data assimilation further leverages the full-field dynamical insights available from climate models to bypass issues related to heterogeneous proxy spatial distribution^{3,4,6–8}. The model ‘prior’ for the assimilation consists of 50-year average states from 17 LGM-to-present time-slice experiments conducted with the isotope-enabled Community Earth System Model version 1 (iCESM1; Extended Data Table 1 and Methods; refs.^{10,22}). We reconstruct climate at 200-year intervals, adhering to the resolution limitations of the majority (>90%) of our proxy data. For a given time interval, we estimate proxy values from the model prior at the locations where geochemical measurements exist using our Bayesian forward models, which take into account seasonal growth preferences on a per-species basis for $\delta^{18}\text{O}_c$ and Mg/Ca (refs.^{20,21}), and seasonal production for U_{37}^K (ref.¹⁹; Methods). The difference between the actual and the forward modelled proxy value (the ‘innovation’) is weighted by the Kalman gain, which considers the covariance between the proxy location and the climate fields as well as uncertainties in the proxies and the prior, producing an ‘update’ that is then added to the model prior state. For our final reconstruction, we generated a posterior ensemble of 500 realizations, based on random sampling of 60 prior states for each time interval, with 20% of proxy records withheld for error quantification and validation testing. We also sampled age uncertainty to ensure that this source of error was propagated into our assimilated fields. As in proxy-only analyses^{3,4,6,7,12}, this results in some temporal smoothing of our LGMR ensemble mean but does not impact the fidelity of millennial-scale trends or features (Methods).

The LGMR highlights the exceptional and spatially heterogeneous nature of deglacial climate change (Fig. 2). Reconstructed GMST

reveals a distinct three-part sequence across the past 24 kyr. From 24–17 ka, the Earth is in a ubiquitously cold glacial state. The thermal imprints of the North American and Eurasian ice sheets are near their maximum extent, with terrestrial cooling relative to the preindustrial below -20°C across the glaciated high northern (>45°N) and southern (>45°S) latitudes (Fig. 2). At 16.9 ka (median; 95% confidence interval (CI) = 18.5–16.0 ka; Supplementary Information), global-scale deglaciation (the second stage) abruptly begins. Deglacial global warming shows a familiar³ two-step rise that is punctuated by the millennial-scale Bølling–Allerød (14.8–12.8 ka) to Younger Dryas (12.8–11.7 ka) events. Following the Younger Dryas cooling event, the Earth enters its final transition towards the present interglacial. In the third part of the GMST sequence, early Holocene (11 ka onward) warming stabilizes by 9.5 ka (11.2–8.7 ka) and is followed by a small (~0.5°C) but significant (>99% probability from 9.5–0 ka) global warming until preindustrial times. A vestigial cold imprint over northeastern North America is all that remains of the once-great Northern Hemisphere ice sheets at 9 ka as mild, albeit widespread, high-latitude warming ensues; Antarctica shows a notable east-west thermal dipole next to a relatively warm Southern Ocean; whereas mild cooling persists across much of the tropics (Fig. 2). All told, we estimate a global warming of $7.0 \pm 1.0^\circ\text{C}$ (2σ) from the deglaciation onset to preindustrial, which is larger than the value reported in ref.¹⁰ (6.1°C), with ~90% of the warming occurring between 16.9 ka and 9.5 ka. The greater warming found here reflects the LGM period referenced (ref.¹⁰ uses 23–19 kyr, which corresponds to $6.8 \pm 1.0^\circ\text{C}$ in the LGMR) as well as differences in iCESM model priors, proxy data distribution, and the degree of covariance localization used (Methods).

Validating the LGMR

Offline data assimilation products are strongly dependent on the covariance structure of the model prior²³. A limitation of the LGMR is that it is based on priors from a single model (iCESM), which are inevitably biased by model deficiencies, resolution and uncertainties in boundary conditions. However, we can objectively test the veracity of the LGMR, including its spatial representation, using two independent methods of statistical validation. First, we use our posterior LGMR fields to reconstruct withheld proxy time series (for example, ref.¹⁷).

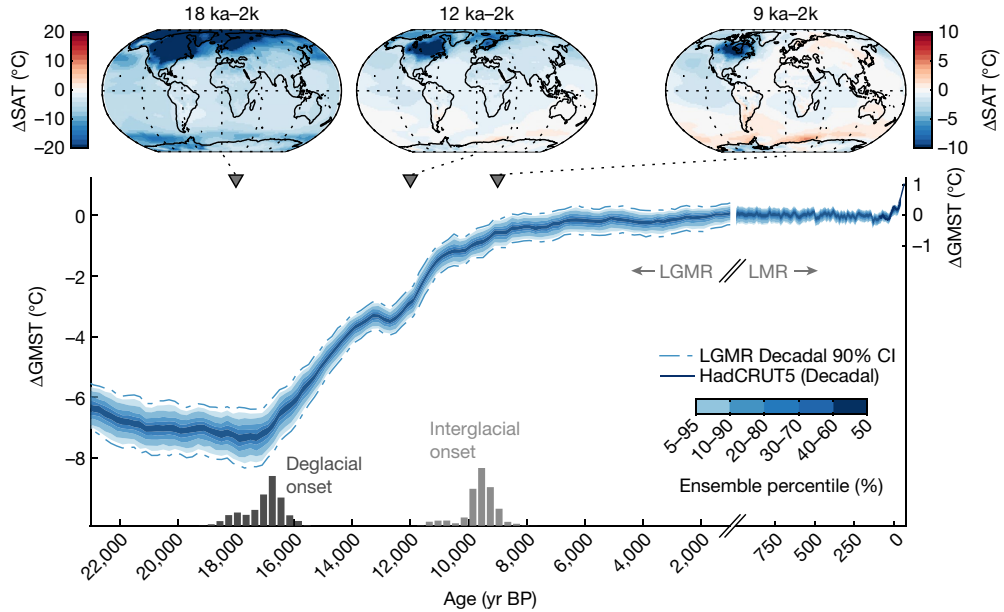


Fig. 2 | Global mean surface temperature change over the past 24 kyr.

Ensemble distribution ($n = 500$ posterior means) of LGMR GMST for the past 24 kyr (blue colours), with a decadal 90th-percentile range (dotted-dashed lines) estimated using decadal-to-centennial variance ratios from iCESM (Methods). Shown at the top are spatial surface air temperature (SAT) anomalies relative to the past two millennia ('2k', 0–2 ka) for intervals discussed in the

main text. The estimated last deglacial and interglacial onset timings are shown as dark and light histograms at the bottom (Supplementary Information). Reconstructed decadal GMST from the last millennium reanalysis v2.1 (ref. ¹⁷) and HadCRUT5 observational product¹¹ are plotted to the right of the LGMR. ΔGMST is computed relative to the preindustrial last millennium average (1000–1850 CE).

Across the ensemble, the majority of records are skilfully reconstructed (Methods) with no obvious signs of regional biasing (Extended Data Fig. 2). Second, following ref. ¹⁰, we compare posterior $\delta^{18}\text{O}$ of precipitation ($\delta^{18}\text{O}_p$) to independent ice core- and speleothem-derived $\delta^{18}\text{O}_p$ time series (Extended Data Table 2). On a global scale, we find notable improvement in the posterior comparison of $\delta^{18}\text{O}_p$ over the modelled state, with a ~30% reduction of error and a large increase in variance explained (Extended Data Fig. 3). LGMR recovers 65–90% of the ice core $\delta^{18}\text{O}_p$ variance ($n = 13$ records; Extended Data Table 2), including divergent Holocene trends in east versus west Antarctica $\delta^{18}\text{O}_p$ (Extended Data Fig. 4). Both tests suggest that our posterior assimilation is robust, but the close correspondence between LGMR $\delta^{18}\text{O}_p$ and ice core proxy records in particular emphasizes that the LGMR is producing a realistic climate state.

Drivers of global temperature change

To gain further insight into the drivers of global surface temperature change during the past 24 ka, we decompose our LGMR temperature fields into spatiotemporal modes of variability using empirical orthogonal function (EOF) analysis (Supplementary Information). As expected, the first spatial mode, EOF1, exhibits positive loading across the globe and explains the majority (>90%) of the surface temperature covariance during the past 24 ka (Fig. 3a). This mode is clearly associated with deglaciation, with the strongest amplitude concentrated atop the North American and Fennoscandian ice sheets. The uniform nature of EOF1 implies an association with changes in greenhouse gas (GHG) radiative forcing and ice sheet albedo. Given the monotonic nature of the associated principal component time series, PC1, GHG forcing²⁴ can explain 92% of the EOF1 variance (Fig. 3b). However, there are notable differences between the two time series: during the early to mid-Holocene, GHG radiative forcing increases at around 12 ka and then gradually decreases, while PC1 steadily increases. This implies GHG forcing alone is not sufficient for explaining the leading mode of global temperature variability.

Modelling experiments indicate that the magnitude of ice sheet albedo forcing is comparable to (if not greater than) GHG forcing across the deglacial transition^{10,13,25}. By considering GHG and ice sheet forcing together, we account for 98% of the variance in PC1 as well as the observed warming during the Holocene (Fig. 3c). The inclusion of ice sheet albedo forcing also explains the strong EOF1 loading atop North America and Fennoscandia (Fig. 3a). Although other radiative forcings, such as vegetation and dust, probably also impacted LGM-to-present temperature change¹⁰ our EOF results imply that these were of lesser importance in terms of their global footprint, particularly during deglaciation.

The second mode of global temperature variability, EOF2, explains only 3.5% of the variance. However, it is distinct from its neighbouring tailoring modes and physically interpretable (Supplementary Information). This mode is a hemispheric dipole, with strong positive loading across the Southern Ocean and negative loading spanning much of the Northern Pacific, North America and the North Atlantic (Fig. 3b). Its associated time series, PC2, consists of both long-term trends as well as millennial-scale peaks during the deglaciation. We interpret this mode to represent a superposition of two sources of climate variability: changes in Atlantic Meridional Overturning Circulation (AMOC; the millennial-scale features) and orbitally induced shifts in high latitude seasonality (the long-term trends). To illustrate this, we decompose PC2 into its long-term 'trend' (Fig. 3c, purple) and millennial-scale 'residual' components (Fig. 3c, yellow).

The trend component of PC2 represents a precession cycle, with a peak at around 11 ka. Both summer insolation intensity at 65°N ²⁶ and Southern Hemisphere summer duration at 65°S ²⁷ offer good approximations of this long-term change (Fig. 3c). However, we interpret the latter as the likely driver. Enhanced summer insolation in the Northern Hemisphere would not cause mean annual cooling; this conflicts with conventional Milankovitch orbital theory²⁸. In addition, spatial correlation analyses (of either orbital series) with surface temperatures indicate that the strongest coupling occurs in the Southern Hemisphere (Extended Data Fig. 5b). The strong loading of EOF2 in the

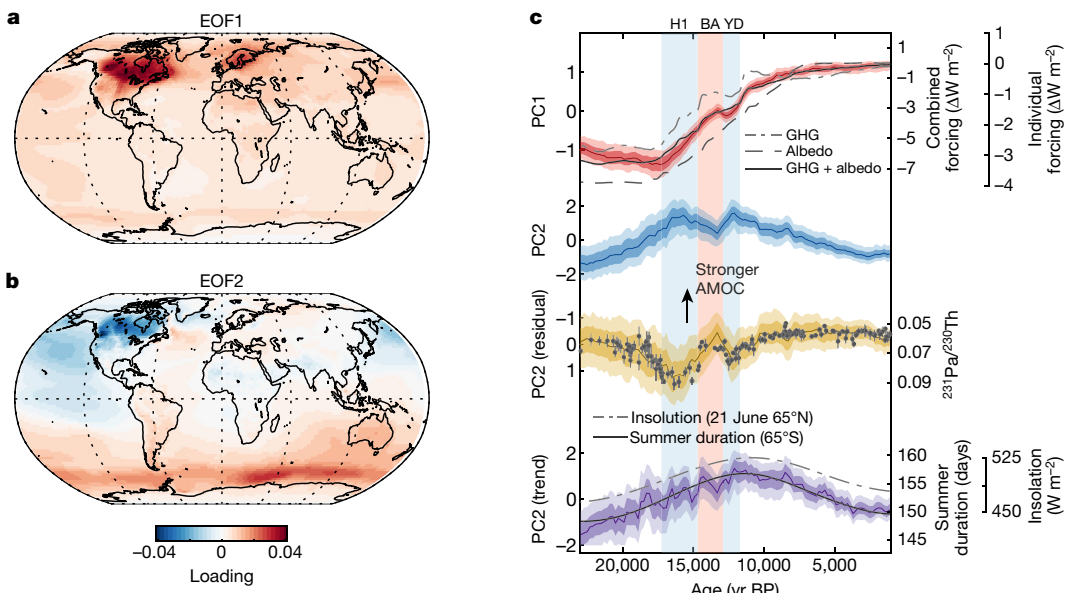


Fig. 3 | Leading modes of LGM-to-present surface temperature variability. **a, b,** Empirical orthogonal function (EOF) 1 and EOF 2 of surface air temperature during the past 24 kyr. **c,** Comparison between the associated principal component time series and climatic drivers. From top: PC1 (red) versus greenhouse gas (GHG) radiative forcing²⁴, albedo radiative forcing (derived following ref. ¹³), and combined GHG and albedo radiative forcing; PC2 (blue); the ‘residual’ component of the regression of 65°S summer duration (the number of days where mean-annual insolation exceeds 250 W m⁻² following ref. ²⁷)

onto PC2 (gold) versus AMOC proxies from the Bermuda Rise ($^{231}\text{Pa}/^{230}\text{Th}$; error bars indicate 2σ uncertainty³¹); the ‘trend’ component of the regression of 65°S summer duration onto PC2 (purple; calculated as the residual of the regression of AMOC proxies onto PC2, to include uncertainties) versus summer solstice 65°N insolation²⁶ and 65°S summer duration. All PC series are in normalized units. Dark and lighter shading on the time series indicate $\pm 1\sigma$ and 95% confidence intervals, respectively. Heinrich event 1 (H1), the Bølling–Allerød (BA) and the Younger Dryas (YD) are also indicated.

Southern Ocean in particular could point towards a feedback with regional sea ice; a longer summer (and shorter winter) would increase the extent of summertime sea ice retreat while decreasing its growth during wintertime, resulting in an increase in mean annual surface temperatures²⁷.

The residual component of PC2 closely follows ($R^2 = 0.80$) $^{231}\text{Pa}/^{230}\text{Th}$ proxy records of AMOC from the Bermuda Rise^{29–31} (Fig. 3c). Prior studies have also identified this ‘bipolar seesaw’ mode^{32,33}, which represents the millennial-scale events that occurred during the last deglaciation (Heinrich event 1, the Bølling–Allerød, and the Younger Dryas). Correlation analysis shows that Northern Hemisphere surface temperatures in LGMR are strongly related to AMOC changes (Extended Data Fig. 5c). A decrease in Atlantic heat transport would also lead to compensating warmth in the Southern Hemisphere, similar to the loading pattern of EOF2. However, the particularly strong loading found across the Indian and Pacific Ocean sectors of the Southern Ocean does not match the classic fingerprint of the oceanic bipolar seesaw³⁴. Similarly, the strong loading in the eastern North Pacific is not typical of a modelled response to an AMOC slowdown^{1,35,36}. It does, however, reflect the underlying proxy records from this region, which show a strong response of SST to North Atlantic climate variability³⁷. Columbia River megaflood meltwater forcing may have contributed to the severe cooling observed in deglacial SST records from the Gulf of Alaska³⁷; however, step-wise deglacial cooling might also be explained by dynamic changes in the subpolar gyre boundary³⁸.

Comparison to proxy-only insights

LGMR GMST shows several notable differences when compared to the proxy-only SMC reconstruction. Focusing first on pre-Holocene differences, the LGMR has a more abrupt onset of deglaciation at ~17 ka, and a more muted Bølling–Allerød–Younger Dryas transition (Fig. 4a). The LGMR also indicates nearly twice as much glacial cooling, but this can be explained by the fact that the SMC is based mostly on SST proxies

and was not scaled to infer GMST; we scale it here for comparison (Fig. 4a). To diagnose the origin of the other differences, we generated a proxy-only GMST reconstruction from our SST compilation (Methods). Even though our compilation has many more proxy SST records (and no terrestrial records), it is strongly correlated with SMC ($R^2 = 0.98$).

The similarity of the proxy-only reconstruction and the SMC illuminates at least two shortcomings that are effectively mitigated by our data assimilation approach. First, proxy-specific GMST reconstructions suggest that the gradual deglacial onset is most likely to be linked to the Mg/Ca data, which show early deglacial SST increases relative to U_{37}^{K} and $^{81}\text{O}_\text{c}$ (Extended Data Fig. 6a and Supplementary Information). Such differences may reflect proxy-specific spatial bias (Fig. 1); data assimilation will mitigate these differences by balancing signals from other nearby proxies. Second, data assimilation allows us to overcome problems associated with spatial aliasing in the proxy distribution. Unlike the enhanced Younger Dryas cooling shown by the proxy-only curves (Fig. 4a), LGMR reveals that Younger Dryas cooling was in fact confined to the Northern Hemisphere (and, specifically, the North Atlantic and North Pacific sectors; Extended Data Fig. 7). Thus, the stronger expression of the Younger Dryas in the proxy-only GMST curves could reflect Northern Hemisphere bias in the proxy distribution during the deglaciation (Fig. 1a).

Holocene global temperature trends

The LGMR provides an updated view of the Holocene temperature conundrum². All of the proxy-only reconstructions—including SMC, Temp12K⁷ and ours—show a cooling trend that begins at ~7 ka BP and continues through the Holocene (Fig. 4b). In contrast, LGMR shows a small (0.25 °C) but significant warming ($P > 0.9$, based on ensemble analysis) since 7 ka (Fig. 4b). The Holocene trend in LGMR does not come from the model prior; in fact, the model suggests a warmer mid-Holocene due to a prescribed ‘Green Sahara’ (Methods; Extended Data Table 1). Rather, it is a feature of the assimilation: the early-mid Holocene warming in Mg/Ca

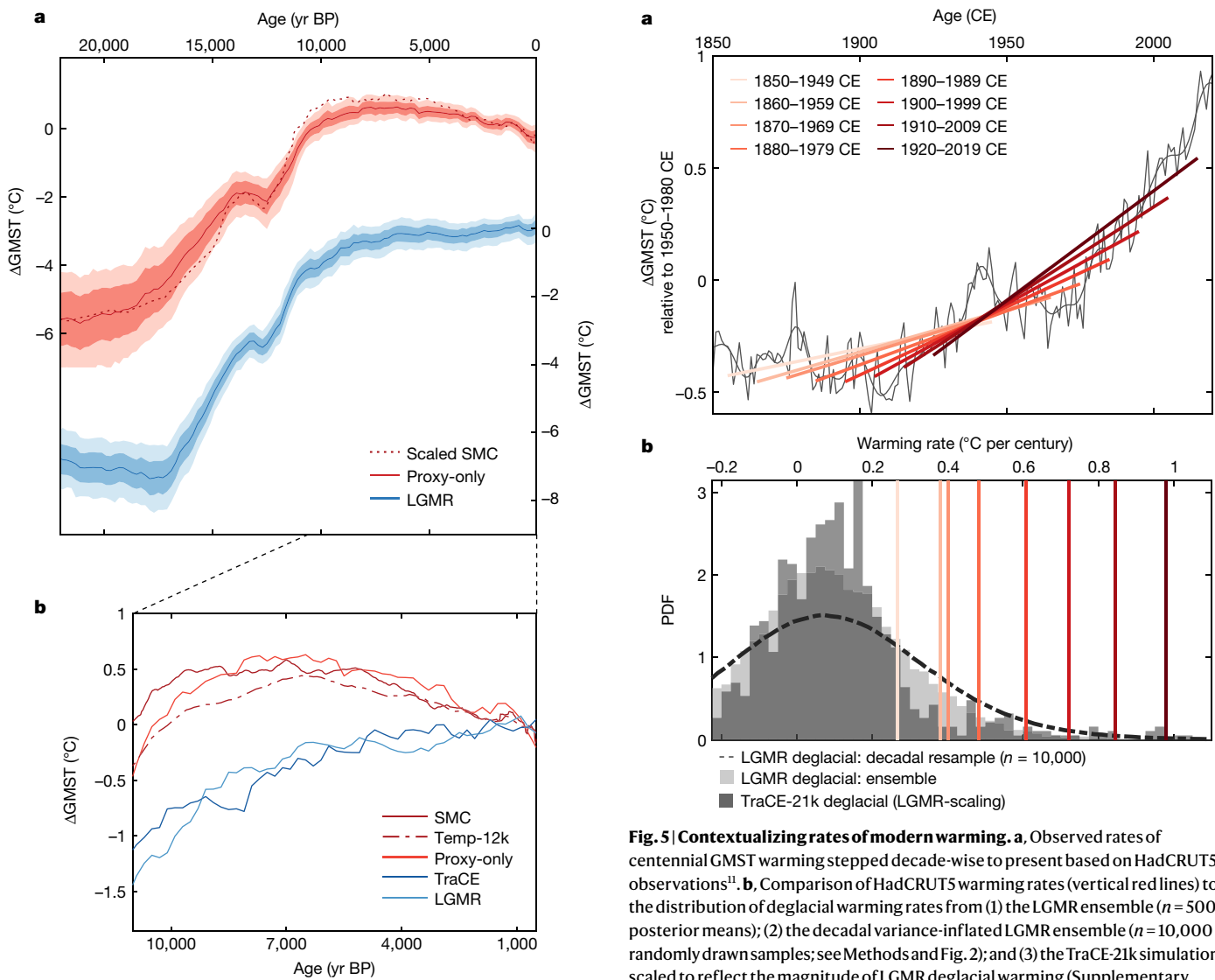


Fig. 4 | Comparison of LGM-to-present surface temperature reconstructions.

a, The proxy-only GMST reconstruction (this study; red) overlain with the GMST-scaled SMC curve (dotted dark red), and LGMR GMST (this study; blue). Uncertainty ranges denote $\pm 1\sigma$ (dark) and 95% confidence intervals (light). All ΔGMST curves are shown as deviations relative to the past two millennia. b, Holocene temperature trends from a alongside the reconstruction of ref. ⁷ ('Temp-12k'; red dotted-dashed) and the TraCE-21k simulation¹.

(and, to a lesser extent, U_{37}^{K} and $\delta^{18}\text{O}_c$) that underlies the conundrum is nearly eliminated after assimilating each proxy type into iCESM (Extended Data Fig. 6). Such consistency implies that a warming trend through the Holocene is a robust solution. This solution is generally similar to the temperature evolution simulated by TraCE-21k (Fig. 4b) indicating that the Holocene conundrum is effectively resolved by data assimilation.

Most likely, this is related to how data assimilation weights the proxies to compute a global average. Data assimilation weights proxies based on their uncertainties and the model-proxy covariance structure and uses this information to update the surface air temperature field. In contrast, proxy-only reconstructions rely on simple latitudinal binning and weighting. This renders the latter approach particularly sensitive to latitudinal bands with sparse proxy coverage or outliers. Sensitivity tests (Supplementary Information) suggest that limited number of proxies in the Southern Ocean latitude band ($45\text{--}60^\circ\text{S}$) can account for about half of the early Holocene warmth in our proxy-only GMST curve (Extended Data Fig. 6b). This implies the Holocene conundrum

Fig. 5 | Contextualizing rates of modern warming. a, Observed rates of centennial GMST warming stepped decade-wise to present based on HadCRUT5 observations¹¹. b, Comparison of HadCRUT5 warming rates (vertical red lines) to the distribution of deglacial warming rates from (1) the LGMR ensemble ($n=500$ posterior means); (2) the decadal variance-inflated LGMR ensemble ($n=10,000$ randomly drawn samples; see Methods and Fig. 2); and (3) the TraCE-21k simulation¹ scaled to reflect the magnitude of LGMR deglacial warming (Supplementary Information). Observed centennial warming rates after 1910 CE exceed the 99th percentiles of the three distributions.

may be, in part, an artifact of poor spatial averaging. More broadly, given that proxies are unevenly distributed, proxy-only reconstructions do not represent a true global average. In contrast, LGMR-based GMST is based on a spatially complete field, and thus is truly a global mean air temperature. This is a clear strength of the LGMR over existing reconstructions.

Proxy seasonal bias may also play a role^{2,8}. The LGMR uses proxy forward models that account for seasonal plankton growth^{19–21} and allow $\delta^{18}\text{O}_c$ and Mg/Ca seasonality to change through time. Our proxy-only curves use inversions of the same models but require that seasonality be temporally fixed. Thus, the proxy-only reconstructions could be more affected by seasonal bias. However, analyses exploring the impact of seasonally biased records, as well as the 'dynamic' seasonality in LGMR, indicate that seasonality has a minimal influence on the Holocene GMST trajectory in both proxy-only reconstructions and data assimilation (Extended Data Fig. 6a–c and Supplementary Information). Within the confines of our forward modelling assumptions, seasonal bias is a less prominent contributor to the conundrum than spatial weighting.

Finally, the LGMR allows us to directly assess 20th and 21st century warming from the broader vantage point of the past 24 kyr. When

juxtaposed alongside the last millennium reanalysis (also a paleoclimate data assimilation product¹⁷) and observational HadCRUT5¹¹ (Fig. 2), we find that 2010–2019 mean GMST exceeds the upper bound (>99.9th percentile) of decadal-estimated values from the LGMR by a considerable margin: >0.5 °C, or +1.5 °C above mean Holocene GMST. These findings differ from those of Marcott et al.⁶, who suggested that early 21st century temperatures (2000–2009) had not yet exceeded early Holocene values and reflect increased confidence over ref.⁷, who find that 2010–2019 warming is at the ~80% CI of mid-Holocene centennial-scale values. Similarly, we find the HadCRUT5-observed rate of 20th to 21st century warming (0.96 °C per century) registers near the upper bound of LGMR deglacial warming rates (that is, >99th percentile; Fig. 5). A similar conclusion is reached when comparing HadCRUT5 warming rates to the monthly resolved TraCE-21k simulation scaled to match the larger magnitude of deglacial warming shown by the LGMR (Fig. 5 and Supplementary Information)^{1,2}. The LGMR underscores the dramatic nature of anthropogenic warming, whose magnitude and rate appear unusual in the context of the past 24 kyr.

Online content

Any methods, additional references, Nature Research reporting summaries, source data, extended data, supplementary information, acknowledgements, peer review information; details of author contributions and competing interests; and statements of data and code availability are available at <https://doi.org/10.1038/s41586-021-03984-4>.

1. Liu, Z. et al. Transient simulation of last deglaciation with a new mechanism for Bølling-Allerød warming. *Science* **325**, 310–314 (2009).
2. Liu, Z. et al. The Holocene temperature conundrum. *Proc. Natl Acad. Sci. USA* **111**, E3501–E3505 (2014).
3. Shakun, J. D. et al. Global warming preceded by increasing carbon dioxide concentrations during the last deglaciation. *Nature* **484**, 49–54 (2012).
4. Snyder, C. W. Evolution of global temperature over the past two million years. *Nature* **538**, 226–228 (2016).
5. Bereiter, B., Shackleton, S., Baggenstos, D., Kawamura, K. & Severinghaus, J. Mean global ocean temperatures during the last glacial transition. *Nature* **553**, 39–44 (2018).
6. Marcott, S. A., Shakun, J. D., Clark, P. U. & Mix, A. C. A reconstruction of regional and global temperature for the past 11,300 years. *Science* **339**, 1198–1201 (2013).
7. Kaufman, D. et al. Holocene global mean surface temperature, a multi-method reconstruction approach. *Sci. Data* **7**, 201 (2020).
8. Bova, S., Rosenthal, Y., Liu, Z., Godad, S. P. & Yan, M. Seasonal origin of the thermal maxim at the Holocene and the last interglacial. *Nature* **589**, 548–553 (2021).
9. Hakim, G. J. et al. The last millennium climate reanalysis project: framework and first results. *J. Geophys. Res. Atmos.* **121**, 6745–6764 (2016).
10. Tierney, J. E. et al. Glacial cooling and climate sensitivity revisited. *Nature* **584**, 569–573 (2020).
11. Morice, C. P. et al. An updated assessment of near-surface temperature change from 1850: the HadCRUT5 dataset. *J. Geophys. Res. Atmos.* **126**, e2019JD032361 (2020).
12. Marsicek, J., Shuman, B. N., Bartlein, P. J., Shafer, S. L. & Brewer, S. Reconciling divergent trends and millennial variations in Holocene temperatures. *Nature* **554**, 92–96 (2018).
13. Baggenstos, D. et al. Earth's radiative imbalance from the Last Glacial Maximum to the present. *Proc. Natl Acad. Sci. USA* **116**, 14881–14886 (2019).
14. Kageyama, M. et al. The PMIP4-CMIP6 Last Glacial Maximum experiments: preliminary results and comparison with the PMIP3-CMIP5 simulations. *Clim. Past* **17**, 1065–1089 (2021).
15. Brierley, C. M. et al. Large-scale features and evaluation of the PMIP4-CMIP6 mid Holocene simulations. *Clim. Past* **16**, 1847–1872 (2020).
16. Park, H.-S., Kim, S.-J., Stewart, A. L., Son, S.-W. & Seo, K.-H. Mid-Holocene Northern Hemisphere warming driven by Arctic amplification. *Sci. Adv.* **5**, eaax8203 (2019).
17. Tardif, R. et al. Last Millennium Reanalysis with an expanded proxy database and seasonal proxy modeling. *Clim. Past* **15**, 1251–1273 (2019).
18. Tierney, J. E. & Tingley, M. P. A Bayesian, spatially-varying calibration model for the TEX₈₆ proxy. *Geochim. Cosmochim. Acta* **127**, 83–106 (2014).
19. Tierney, J. E. & Tingley, M. P. BAYSPLINE: a new calibration for the alkenone paleothermometer. *Paleoceanogr. Paleoclimatol.* **33**, 281–301 (2018).
20. Malevich, S. B., Vetter, L. & Tierney, J. E. Global core top calibration of δ¹⁸O in planktic foraminifera to sea surface temperature. *Paleoceanogr. Paleoclimatol.* **34**, 1292–1315 (2019).
21. Tierney, J. E., Malevich, S. B., Gray, W., Vetter, L. & Thirumalai, K. Bayesian calibration of the Mg/Ca paleothermometer in planktic foraminifera. *Paleoceanogr. Paleoclimatol.* **34**, 2005–2030 (2019).
22. Brady, E. et al. The connected isotopic water cycle in the community Earth system model version 1. *J. Adv. Model. Earth Syst.* **11**, 2547–2566 (2019).
23. Amrhein, D. E., Hakim, G. J. & Parsons, L. A. Quantifying structural uncertainty in paleoclimate data assimilation with an application to the last millennium. *Geophys. Res. Lett.* **47**, e2020GL090485 (2020).
24. Köhler, P., Nehrbass-Ahles, C., Schmitt, J., Stocker, T. F. & Fischer, H. A 156 kyr smoothed history of the atmospheric greenhouse gases CO₂, CH₄, and N₂O and their radiative forcing. *Earth Syst. Sci. Data* **9**, 363–387 (2017).
25. Braconnot, P. & Kageyama, M. Shortwave forcing and feedbacks in Last Glacial Maximum and Mid-Holocene PMIP3 simulations. *Philos. Trans. R. Soc. A* **373**, 20140424 (2015).
26. Berger, A. Long-term variations of daily insolation and quaternary climatic changes. *J. Atmos. Sci.* **35**, 2362–2367 (1978).
27. Huybers, P. & Denton, G. Antarctic temperature at orbital timescales controlled by local summer duration. *Nat. Geosci.* **1**, 787–792 (2008).
28. Imbrie, J. et al. On the structure and origin of major glaciation cycles I. Linear responses to Milankovitch forcing. *Paleoceanography* **7**, 701–738 (1992).
29. McManus, J. F., Francois, R., Gherardi, J.-M., Keigwin, L. D. & Brown-Leger, S. Collapse and rapid resumption of Atlantic meridional circulation linked to deglacial climate changes. *Nature* **428**, 834–837 (2004).
30. Böhm, E. et al. Strong and deep Atlantic meridional overturning circulation during the last glacial cycle. *Nature* **517**, 73–76 (2015).
31. Lippold, J. et al. Constraining the variability of the Atlantic meridional overturning circulation during the Holocene. *Geophys. Res. Lett.* **46**, 11338–11346 (2019).
32. Shakun, J. D. & Carlson, A. E. A global perspective on Last Glacial Maximum to Holocene climate change. *Quat. Sci. Rev.* **29**, 1801–1816 (2010).
33. Clark, P. U. et al. Global climate evolution during the last deglaciation. *Proc. Natl Acad. Sci. USA* **109**, E1134–E1142 (2012).
34. Pedro, J. B. et al. Beyond the bipolar seesaw: toward a process understanding of interhemispheric coupling. *Quat. Sci. Rev.* **192**, 27–46 (2018).
35. He, F. et al. Northern Hemisphere forcing of Southern Hemisphere climate during the last deglaciation. *Nature* **494**, 81–85 (2013).
36. Ritz, S. P., Stocker, T. F., Grimalt, J. O., Menviel, L. & Timmermann, A. Estimated strength of the Atlantic overturning circulation during the last deglaciation. *Nat. Geosci.* **6**, 208–212 (2013).
37. Praetorius, S. K. et al. The role of Northeast Pacific meltwater events in deglacial climate change. *Sci. Adv.* **6**, eaay2915 (2020).
38. Gray, W. R. et al. Wind-driven evolution of the North Pacific subpolar gyre over the last deglaciation. *Geophys. Res. Lett.* **47**, e2019GL086328 (2020).

Publisher's note Springer Nature remains neutral with regard to jurisdictional claims in published maps and institutional affiliations.

© The Author(s), under exclusive licence to Springer Nature Limited 2021

Methods

Proxy compilation and screening

We collated a globally dispersed set of 573 SST proxy records spanning the past 24 kyr. Following ref.¹⁰, we focus on geochemical proxies for SST including alkenone U₃₇^K (146 records), the TetraEther indeX of 86 carbons (TEX₈₆; 28 records), the elemental ratio of Mg to Ca in planktic foraminifera (Mg/Ca; 129 records), and the oxygen isotopic composition of planktic foraminifera ($\delta^{18}\text{O}_c$; 270 records). As in ref.¹⁰, we limit our analyses to these proxies because we have already developed Bayesian forward models for each of them^{18–21} that we can use in our paleoclimate data assimilation scheme (see the ‘Paleoclimate data assimilation’ section below). These data tend to cluster along coasts where sedimentation rates are high, and in regions where sampling efforts have historical focused (for example, the Atlantic sector and Northern Hemisphere). By comparison, data coverage across ocean interiors—in particular, the Pacific and (to a lesser extent) Southern Oceans—is sparse. For consistency, we recalibrated all age models using the Marine13 radiocarbon calibration curve³⁹ with the BACON age model program⁴⁰ and local estimates of deviations from the global marine radiocarbon reservoir age (ΔR). This procedure also allowed us to generate ensembles ($n = 1,000$) of possible age models for each record that were used to propagate dating uncertainties into our data assimilation product (see sections ‘Paleoclimate data assimilation’ and ‘Proxy-only global mean temperature’ below).

Some screening of our proxy compilation was necessary to remove low-resolution, short and adversely situated proxy records. Generally speaking, we removed records whose median age resolution was less than 1,000 years or were less than 4,000 years long (Extended Data Fig. 1). However, the former constraint was relaxed for records situated in or near the Southern Ocean, where data coverage is sparse, so as to retain as many time series as possible from this undersampled region. To remove anomalous influences of sea ice on our proxy estimates (in particular, the influence of sea ice on the $\delta^{18}\text{O}$ of seawater²⁰) we removed records situated at locations where preindustrial mean annual SSTs were less than 0 °C (a value assumed to roughly approximate the perennial sea ice edge), as estimated from the World Ocean Atlas 2013 product⁴¹. This resulted in 4 $\delta^{18}\text{O}_c$ records being removed from locations each north of 80°N. Following ref.¹⁹, we also omitted all U₃₇^K records situated north of 70°N or within the modern Arctic sea ice zone, due to known biases in the alkenone temperature proxy that are likely to arise from lipid contributions from Isochrysidales species living in sea ice⁴². We also removed two western Atlantic sites, OCE326-GGC26 (43°29'N, 54°52'W) and OCE326-GGC30 (43°53'N, 62°48'W; ref.⁴³). While these U₃₇^K records have been featured in prior mean global Holocene temperature reconstructions⁶, they show an extremely large (up to 10 °C) cooling over the Holocene that most likely reflects a shift in the Gulf Stream/Labrador Current boundary⁴³. This poses a problem for our data assimilation technique, because CESM1.2 does not put this sharp boundary in the same place as observations. Assimilation of these sites thus has a tendency to cause a large regional bias in SSTs. Although similar issues arising in part from coarse model resolution probably afflict other frontal regions, no sufficient cause was found to warrant the removal of any additional records. All told, our selection criteria resulted in the removal of 34 records.

Proxy-only global mean temperature reconstruction

To provide a point of comparison for our data assimilation results, we generated a reconstruction of global mean temperature change using only the proxy data, broadly following the methodology of ref.⁴⁴. This was done by first estimating a ‘reference’ preindustrial proxy value for each site and then appending each value at the top of its respective $N \times 1$ proxy record. This produced an $(N_i + 1) \times 1$ vector

of proxy values for each site i , where the +1 denotes the appended preindustrial reference value. For sites with value(s) overlapping the preindustrial (that is, 0–4 kyr BP; see ref.¹⁰), the preindustrial reference was computed as the 0–4 kyr mean proxy value. For sites without preindustrial overlap, reference proxy values were estimated by using the nearest core-top value^{18–21}. As in ref.⁴⁴, if no core-top locations existed within a threshold 300 km radius, an observational preindustrial SST estimate was taken from the HadISST product⁴⁵ and forward modelled to a proxy estimate. All $(N_i + 1) \times 1$ vectors were then calibrated to SSTs using the Bayesian inverse models^{18–21}. For the $\delta^{18}\text{O}_c$ and TEX₈₆ models^{19,20} we used prior standard deviation values of 10 °C, while for the U₃₇^K and Mg/Ca models^{18,21} we used values of 5 °C and 6 °C, respectively. All prior standard deviation values are conservative, and only minimally impact the posterior. The Mg/Ca model, BAYMAG, also requires constraints on salinity, pH and bottom water calcite saturation (Ω). The BAYMAG package includes functions to estimate past changes in salinity and pH. Briefly, following refs.^{21,46}, these functions scale the global sea level curve⁴⁷ to an inferred LGM global change of 1.1 psu, then add this to the modern mean annual value of surface salinity for each site, as estimated from the World Ocean Atlas 2013⁴¹. Similarly, to estimate changes in pH, BAYMAG scales the ice core CO₂ record^{48–53} to an inferred global increase of 0.13 pH units during the LGM, and then adds this curve to the modern mean annual value of surface pH estimated from the Global Ocean Data Analysis Project version 2 (GLODAPv2⁵⁴). Following ref.²¹, Ω is estimated at each record’s bathymetric depth using the GLODAPv2 product and assumed to be constant through time. The $\delta^{18}\text{O}_c$ model, BAYFOX, requires constraints on the time-evolution of $\delta^{18}\text{O}$ of seawater ($\delta^{18}\text{O}_{\text{sw}}$). For this, we first scaled the benthic stack of ref.⁵⁵ to an estimated change in global $\delta^{18}\text{O}_{\text{sw}}$ (arising from changes in global ice volume) of +1‰ at the LGM (18 ka) relative to the preindustrial following ref.⁵⁶. This scaled curve was then added to the modern mean annual $\delta^{18}\text{O}_{\text{sw}}$ value⁵⁷ and interpolated in time for each site.

The posterior SST estimates produced by the Bayesian inverse models are a matrix of dimension $(N_i + 1) \times M$, where M contains 1,000 possible SST histories and core-top reference values for each time entry $N_i + 1$ of each i site. These matrices were sorted from least to greatest along dimension M , which preserves the ‘shape’ of the time series, after which a normally distributed analytical uncertainty of $\mathcal{N}(0, 0.5)$ was added back to the sorted ensembles to account for laboratory precision (see also refs.^{10,44}). Finally, we converted each of our records to SST anomaly units relative to preindustrial values by subtracting the first row of the $(N_i + 1) \times M$ matrix (the preindustrial core-top estimate) from the remaining rows to generate an $N_i \times M$ matrix of SST anomalies.

To produce a GMST anomaly curve, SST anomaly values and associated ages were randomly drawn from our ensemble of M posterior values and our ensemble of 1,000 age models, respectively, and then sorted into contiguous 200-year bins spanning back to 24 ka. If more than one data point per record occurred in a given 200-year bin, those SST data points were averaged, to ensure that higher-resolution records did not bias the bin. Following refs.^{4,10,58}, the data within each time bin were binned by latitude, with the bin size randomly selected between 2.5 and 20, and then global average SST (GSST) was computed as the latitudinally weighted zonal average between 60°S and 60°N. Following refs.^{4,10}, GSST was then scaled by a value randomly chosen between 1.5 and 2.3 to transform the values to GMST. This Monte Carlo process was repeated 10,000 times, to propagate errors arising from the SST estimation, age modelling, latitudinal weighting, and GSST to GMST scaling.

Climate model simulations

The climate model priors are drawn from newly developed and pre-existing climate simulations with the water isotope-enabled Community Earth System Model, versions 1.2 and 1.3 (iCESM1.2 and

Article

iCESM1.3). CESM1.2 is an updated version of CESM1⁵⁹, and CESM1.3 contains further updates to the gravity wave scheme, cloud microphysics, and radiation⁶⁰. Critical for our purposes, iCESM explicitly simulates the transport and transformation of stable water isotopes (for example, H₂O, HDO) in all of the component models, and has been shown to reproduce key features of climate and isotopes in present day and paleoclimate observations²². All of the iCESM simulations have a horizontal resolution of 1.9 × 2.5 (latitude × longitude) in the atmosphere and land, and a nominal 1° in the ocean. Pre-existing iCESM simulations used in this study include the preindustrial and LGM simulations with iCESM1.3⁶¹, the preindustrial, 3 ka, 18 ka and LGM simulations with iCESM1.2²⁰, and the last millennium simulation with iCESM1.2⁶² (Extended Data Table 1).

In addition, we developed new time-slice simulations using iCESM1.2 of 16, 14, 12, 9 and 6 ka (Extended Data Table 1). For each time slice, the greenhouse gases (CO₂, CH₄ and N₂O) were set to 200-year averages centred around the corresponding time from ice core reconstructions^{63–65}. Orbital parameters followed ref.²⁶. Ice sheet forcing was prescribed according to the ICE-6G reconstruction⁶⁶, including effects from changes in land elevation and surface properties and the land-sea mask due to sea-level variations. For each time-slice simulation, ocean temperature and salinity were initialized from published CESM1.2 simulations when available⁶⁷. δ¹⁸O_{sw} was initialized from the slice before, for example, δ¹⁸O_{sw} of 18 ka branched from 21 ka. A spatially uniform correction was applied to salinity and δ¹⁸O_{sw} to account for the ice-volume effect. The correction terms were derived by scaling changes in the global volume-mean salinity and δ¹⁸O_{sw} between 21 and 0 ka by the corresponding change in the global mean sea level⁴⁷. Global volume-mean salinity and δ¹⁸O_{sw} were 34.7 and 35.7 g kg⁻¹ and 0.05 and 1.05‰ in the 0 and 21 ka simulations, respectively⁶⁸. The iCESM1.2 time-slice simulations used preindustrial aerosol emissions because of the lack of reliable global reconstructions⁶⁹. For a similar reason, the simulations used the preindustrial vegetation cover except for the 9 and 6 ka slices (see description below). All these time-slice simulations were run for 900 years.

A Green Sahara was implemented in both the 9 and 6 ka simulations by prescribing a 100% spatial coverage of shrub and C4 grass at 10–25°N and 25–35°N, respectively. In addition, C3 grass over the Northern Hemisphere high latitude regions (northward of 50°N) was replaced with boreal trees in the 6 ka simulation. These vegetation changes were developed following recommendations from the Paleoclimate Modeling Intercomparison Project and represent maximum possible vegetation expansion over the Sahara and the Northern Hemisphere according to the pollen and macro-fossil evidence⁷⁰. To sample the uncertainty from vegetation, an additional 6 ka simulation was performed for 400 years with the preindustrial vegetation cover, as another end-member of the mid-Holocene vegetation forcing. All the iCESM1.2 time-slice simulations were run with a prescribed satellite phenology in the land model due to the overall poor simulation of vegetation processes with a prognostic phenology⁷¹. The satellite observation derived vegetation phenology included leaf area and stem area indices, and vegetation heights.

In addition, two water hosing experiments were performed within the 16 and 12 ka slices, respectively, to provide prior climate states for the millennial-scale events of the last deglaciation (that is, Heinrich 1 and the Younger Dryas). In the hosing experiments, 0.25 Sv (1 Sv = 10⁶ m³ s⁻¹) of freshwater with a δ¹⁸O composition of -30‰ (VSMOW) were applied over the northern North Atlantic (50–70°N). These experiments were run for 200 years. AMOC is largely shut down after 100 years in the water hosing simulations with a maximum transport at 34°S reduced to ~3 Sv from a background value of -18 Sv.

Prior to using the simulations in our data assimilation, a paleoclimate calendar adjustment was applied to the monthly model output for all time slices to account for the effect of changing months on seasonal climatic expressions⁷².

Paleoclimate data assimilation

The data assimilation method incorporates an offline ensemble square root Kalman filter approach, following the methodology of ref.¹⁰ using the data assimilation MATLAB code package DASH version 3.6.1 (source code available at <https://github.com/JonKing93/DASH>). We refer the reader to this previous work for a full mathematical description. Briefly, the method combines a set of prior climate states from our model simulations (X_{prior}) with new information from the proxy observations (the ‘innovation’, $y_{\text{obs}} - Y_{\text{est}}$) to compute a ‘posterior’ matrix of assimilated past climate states, X_{post} . The posterior mean and deviations from the mean are each computed separately (see refs.^{10,73}); the Kalman filter mean ‘update’ equation is:

$$\bar{X}_{\text{post}} = \bar{X}_{\text{prior}} + K(y_{\text{obs}} - \bar{Y}_{\text{est}}). \quad (1)$$

\bar{X}_{prior} is an $N \times M$ matrix of prior climate states from iCESM, where dimension N contains the model grid point data for SST and SSS (both at monthly and mean-annual resolution), and mean-annual surface air temperature (SAT), δ¹⁸O_{sw}, precipitation amount-weighted δ¹⁸O (δ¹⁸O_p), and mean-annual precipitation rate collapsed into a concatenated vertical ‘state vector’, and dimension M represents the number of state vector ensemble members; the overbar in all cases denotes averaging across the ensemble dimension (producing, in this case, a vectorized ensemble ‘mean’ update⁷³).

The $P \times 1$ vector y_{obs} consists of P globally dispersed δ¹⁸O_c, Mg/Ca, U₃₇^K and TEX₈₆ proxy observations. The $P \times M$ matrix Y_{est} contains the corresponding set of P proxy estimates, generated from the model output from each M state using our Bayesian forward models. For details concerning the Bayesian models, the readers are referred to the original publications^{18–21}. In brief, the forward model for δ¹⁸O_c requires monthly SST and mean annual δ¹⁸O_{sw}. These δ¹⁸O_c values are computed on a species- and growing season-specific basis²⁰ that allows us to explicitly account for foraminiferal seasonal preferences in our forward model proxy estimates. Both the U₃₇^K and TEX₈₆ models require only SST as inputs, with the former requiring monthly SST due to the seasonal response of U₃₇^K production in the North Pacific, the North Atlantic and the Mediterranean¹⁹, and the latter only mean annual SST¹⁸. Finally, the forward model for Mg/Ca requires both monthly SST and SSS to compute species-specific growing season Mg/Ca values, in addition to sea surface pH, bottom water calcite saturation state (Ω), and the laboratory cleaning method. The latter is provided in the original publications, and SST and SSS are drawn from iCESM output. For pH and Ω , we follow the same procedure as the proxy-only reconstruction (described above).

The innovation ($y_{\text{obs}} - Y_{\text{est}}$) represents the new information from the observations not already provided by the prior estimates. As shown in equation (1), these values are weighted by the $N \times P$ matrix K , the Kalman gain, which takes the general form:

$$K = \text{cov}(X_{\text{prior}}, Y_{\text{est}}) \times [\text{cov}(Y_{\text{est}}, Y_{\text{est}}) + R]^{-1} \quad (2)$$

where ‘cov’ denotes the covariance expectation (approximated by an ensemble mean, with the ensemble mean removed). The $P \times P$ matrix R prescribes the error covariance associated with each proxy observation. Thus, the Kalman gain weights the innovation by the covariance of the forward-modelled proxy estimates with the prior climate states and the uncertainties of the prior-estimated proxy ensemble and the proxy observations. In our case, R is diagonal, that is, the errors are presumed to be independent. R is user-defined, but ideally based on an estimate of ‘true’ proxy uncertainties. Following ref.¹⁰, in which the impact of different values of R on the posterior were systematically tested, we use the error values output from our Bayesian forward models scaled by 1/5, but further refine this by specifying a slightly different scaling factor for each proxy type. To determine these proxy-specific

factors, for each record we performed jack-knife (leave one record out) and ‘only-one record’ assimilation experiments (no R scalings applied) to assess the ability of any particular record to predict all others when that record was either removed, or solely retained, respectively. From these experiments, we then ranked each record by validating the only-one and all-but-one reconstructions against the non-assimilated proxies. This allowed assessment for the percent of tests for which this proxy resulted in ‘improvement’ (as denoted by the ratio of the posterior to prior squared error of all predicted, independent proxies, where a ratio less than unity indicates improvement). Using these rankings for each proxy type, we then weighted each proxy-specific scaling factor by the improvement factor, and subsequently weighted these rankings by total record count to maintain an average R scaling of 1/5 across all available proxy records. The specific scaling factors that we calculated were $r_{\text{uk}} = 3.13^{-1}$, $r_{\text{tex}} = 1.36^{-1}$, $r_{\text{mgca}} = 2.86^{-1}$ and $r_{\text{iso}} = 7.27^{-1}$, indicating $\delta^{18}\text{O}_{\text{C}}$ to be the most reliable (and numerous) proxy type.

Following refs.^{10,17}, we applied covariance localization to the assimilation to limit spurious relationships between proxies and far-field regions. Validation testing suggested that a 24,000 km localization radius provided optimal posterior results for our dataset (see the ‘Internal and external validation testing’ section below). This differs from ref.¹⁰, which used a narrower 12,000 km localization. The improvement we find using broader localization is likely to relate to the fact that fewer proxies are assimilated here per time step than in ref.¹⁰.

For computing our full 24 kyr LGMR product, we calculated \bar{X}_{post} at 200-year increments using the following approach. First, we selected 80% of our proxy records at random for inclusion in our assimilation, with the remaining 20% of records withheld for statistical validation (see the ‘Internal and external validation testing’ section below). For each record, we randomly prescribed an age scale by drawing from the 1,000 viable posterior BACON-derived age models. Second, for each 200-year interval, y_{obs} was compiled as all of the available proxy data points whose ages are within the bounds of the current reconstruction age interval. When multiple data points from a single record occurred within a given 200-year age-interval, these values were averaged. We then randomly selected $M = 60$ state vector ensembles from the iCESM output using a transient ‘evolving prior’ approach (see below) and used the Bayesian forward models to produce the matrix Y_{est} . \bar{X}_{post} was then computed from y_{obs} and Y_{est} (equation (1)) with R in the Kalman gain (equation (2)) scaled to the appropriate proxy type. Finally, this process was repeated for a total 500 times for each time interval, to create a 500-member LGM-to-present ensemble of posterior states. This Monte Carlo procedure ensures that proxy, age-model and model prior uncertainties are included in the assimilated product. Since the proxy age model uncertainties in particular can be on the order of centuries (interquartile range of ~320–770 years across all data points), this sampling procedure has the effect of smoothing the posterior ensemble mean time series on sub-millennial timescales, as in prior proxy-only analyses^{3,4,6}.

Assimilation of the LGM-to-present climate evolution at 200-year intervals directly reflects our underlying proxy data compilation. ~96% of the proxy records have a median resolution that is higher than 200 years (Extended Data Fig. 1). However, if all >60,000 compiled data points are considered together, >90% of the paleoclimate data have sample resolutions of ≤200 years. While ideally, the amount of time represented by the model prior would also equal 200 years, this would have considerably limited the number of model priors available (a maximum of 58 prior states across our all iCESM time-slice simulations, and as few as four priors for a given interval; Extended Data Table 1). To increase the number of iCESM priors available for assimilating our marine proxies while still roughly adhering to our reconstruction interval, we instead used 50-year average priors, following ref.¹⁰. Prior experimentation by ref.¹⁰ showed only marginal differences in LGM and preindustrial posteriors once time-averaging of our iCESM prior fields exceed interannual time periods, justifying this choice.

Assimilating Earth’s transient climate evolution between two fundamentally different glacial versus interglacial states presents a unique obstacle for offline paleoclimate data assimilation (which has largely focused on reconstructing the climate evolution of the Common Era¹⁷, a relatively stable background climate state⁹). In terms of Bayesian inference, the challenge is adequately assigning a collection of iCESM priors at each LGM-to-present reconstruction interval that reflects a reasonable prior belief in their viability. For example, a time interval in the late Holocene should not include glacial prior states that contain a Laurentide ice sheet, as the latter induces fundamental changes in spatial covariance that are not realistic for a deglaciated climate state. Conversely, deglacial prior states might include a range of possible Laurentide configurations.

To address this issue, we developed an ‘evolving prior’ approach. For each 200-year interval, we defined a normal probability density function (PDF) with a 1σ range of 4,000 years and a maximum cut-off range of 3σ ($\pm 12,000$ years). The PDF is truncated to the range of our target time interval (24–0 ka), such that for the tail ends of the reconstruction interval, the PDF ends up being half-normal. We then sampled 60 prior ages from this PDF and rounded them to 0, 3, 6, 9, 12, 14, 16, 18 or 21 ka, the discrete time-slice intervals at which iCESM simulations are available (Extended Data Table 1). For each randomly drawn and rounded age, a model prior was selected (with replacement) from its corresponding iCESM time-slice simulation.

The 1σ range of 4,000 years was chosen to balance the need to include adequate variability in the prior while still excluding model priors that are not physically justified (that is, the inclusion of LGM priors when assimilating mid-late Holocene climatic states, and vice-versa). Similar to ref.¹⁰, rank histogram analysis of our withheld validation proxies⁷⁴ suggested minimal mean bias of our model priors using this 1σ length scale, but an apparent lack of structural variance (as suggested by a U-shaped rank histogram; see Extended Data Fig. 2 of ref.¹⁰). While increasing the length scale to include a broader range of priors would increase prior variance, validation testing indicated that the 4,000-year length scale was near-optimal, and also resulted in substantial improvement over an ‘agnostic’ prior sampling scheme (for example, one that assigns equal probability of including a prior from any given iCESM timeslice; see the ‘Internal and external validation testing’ section below). We note that the variance in our model prior is fundamentally restricted by the use of a sole model (iCESM). Further work is needed to test the sensitivity of the LGMR reconstruction to the use of different isotope-enabled model priors (once available).

Internal and external validation testing

Statistical validation and tuning of our LGMR product was conducted in two ways, referred hereafter as ‘internal’ and ‘external’ validation. The first approach (‘internal’ validation) involves withholding 20% of the marine proxies per iteration (see the ‘Paleoclimate data assimilation’ section above), and then using the posterior SST, SSS and $\delta^{18}\text{O}_{\text{sw}}$ fields to forward model these withheld proxy records. These predicted proxy records were then compared with the actual proxy records using standard skill diagnostics: the coefficient of efficacy (CE; a value between $-\infty$ and 1, where a value >0 is conventionally taken to represent skill over climatology), the squared Pearson product moment coefficient (R^2), and the root mean square error of prediction (RMSEP). The computation of multiple posterior ensembles (that is, $N = 500$), each with 20% withholding, implies each proxy record was randomly withheld and internally validated on average 100 times. These tests yield, on average, CE values that are greater than 0 with no obvious signs of systematic spatial biasing, indicative of skill in our posterior assimilation above our evolving iCESM prior fields. On a global basis all posterior-predicted proxies exhibit a strong correspondence to observed values with $R^2 > 0.95$ and slopes within 5% of their respective 1:1 lines (Extended Data Fig. 2), indicating a lack of systematic bias in the LGMR oceanic climatologies.

Article

Following ref.¹⁰, we also use independent ice core and speleothem records of $\delta^{18}\text{O}_p$ to externally validate the LGMR. In this more stringent analysis, we compare posterior $\delta^{18}\text{O}_p$ to published ice core $\delta^{18}\text{O}$ (which is taken as a direct indicator of precipitation-weighted mean-annual $\delta^{18}\text{O}_p$, given that post-depositional processes such as isotopic diffusion⁷⁵ and sublimation⁷⁶ do not typically impact ice core record integrity across centennial and longer time scales) and speleothem $\delta^{18}\text{O}$, which is first converted to $\delta^{18}\text{O}_p$ via the methodology of ref.⁷⁷ (see also ref.¹⁰). For the speleothem data, we used the SISAL version 1b database⁷⁸. Records were included in our compilation solely on the basis that they span at least 18 kyr: that is, at least three-quarters of the LGMR reconstruction interval, ensuring overlap with the deglacial period (around 17–9 ka; Fig. 2). Record-specific details are provided in Extended Data Table 2. Following ref.¹⁰, we focus on $\delta^{18}\text{O}_p$ deviations ($\Delta\delta^{18}\text{O}_p$), which we generate by differencing all $\delta^{18}\text{O}_p$ values at each time slice interval relative to the 0 ka baseline. This approach is premised on the expectation that $\delta^{18}\text{O}_p$ deviations should be adequately captured by LGMR¹⁰ despite known mean $\delta^{18}\text{O}_p$ biases in iCESM²². We then compare both prior and posterior $\Delta\delta^{18}\text{O}_p$ with observed $\Delta\delta^{18}\text{O}_p$ at the iCESM timeslice intervals (3, 6, 9, 12, 14, 16, 18 and 21 ka) using our statistical diagnostics of covariance and prediction error (R^2 and RMSEP). Positive ΔR^2 (that is, a stronger relationship with observed values in LGMR versus the prior) and negative ΔRMSEP (that is, reduced prediction error in LGMR versus the prior) imply improvement in our LGMR posterior relative to the iCESM priors.

Overall, this external validation test indicates that LGMR substantially improves over the prior, with a nearly 30% error reduction ($\text{RMSEP}_{\text{prior}} = 2.60\%$; $\text{RMSEP}_{\text{posterior}} = 1.92\%$) and approaching two times greater variance explained in with our posterior-predicted values relative to the prior ($R^2_{\text{prior}} = 0.37$; $R^2_{\text{posterior}} = 0.62$). Although much of the improvement is driven by ice core $\Delta\delta^{18}\text{O}_p$ estimates (Extended Data Figs. 3 and 4), offsets with speleothem $\Delta\delta^{18}\text{O}_p$ observations are also strongly reduced in LGMR relative to iCESM. The comparably poor temporal covariance shown by global speleothem $\Delta\delta^{18}\text{O}_p$ values relative to ice cores (Extended Data Fig. 4; Extended Data Table 2) may reflect local-scale influences on speleothem $\Delta\delta^{18}\text{O}_p$ records, such as groundwater storage, mixing, recharge and residence time variations; subgrid-scale topographic and (or) precipitation influences; and uncertainties arising from indirectly inferring $\delta^{18}\text{O}_p$ from $\delta^{18}\text{O}_{\text{calcite}}$ or $\delta^{18}\text{O}_{\text{aragonite}}$ measurements⁷⁷. In addition, the iCESM prior range of $\delta^{18}\text{O}_p$ across the LGM to present in the tropics is considerably smaller than in the high latitudes (for example, Extended Data Fig. 4), which might restrict the posterior solutions for the speleothems (see ref.¹⁰).

We used external validation testing to choose both the covariance localization radius and evolving prior 1σ range (see the ‘Paleoclimate data assimilation’ section for a description of each). Between the two, our tests show that LGMR is most sensitive to the choice of localization radius. We tested values between 6,000 km and infinite (that is, no localization) and found a relatively broad localization cut-off (24,000 km) is near-optimal (Extended Data Table 3). In contrast, LGMR shows comparably less sensitivity to choice of the 1σ range for sampling iCESM priors, with acceptable external validation scoring for values between $1\sigma = 2,000$ –6,000 years (Extended Data Table 3). For our final LGMR product we chose a value of $1\sigma = 4,000$ years as this was shown to provide near-optimal validation scoring (Extended Data Table 3), while also constituting a reasonable ‘middle ground’ between enabling adequate variance amongst iCESM model priors throughout the past 24 kyr while excluding physically unjustifiable states (see discussion above).

Data availability

All LGMR and associated proxy data are publicly available via the National Oceanic and Atmospheric Administration (NOAA) Paleoclimatology Data Archive (<https://www.ncdc.noaa.gov/paleo/study/33112>). Source data are provided with this paper.

Code availability

The MATLAB code used for the reconstruction (DASH) are publicly available (<https://github.com/JonKing93/DASH>), as are all accompanying Bayesian proxy forward models (BAYSPAR, BAYSPLINE, BAYFOX, and BAYMAG) used in this study (<https://github.com/jesstierney>). The iCESM1.2 model code is available at <https://github.com/NCAR/iCESM1.2>.

39. Reimer, P. J. et al. IntCal13 and Marine13 radiocarbon age calibration curves 0–50,000 years cal BP. *Radiocarbon* **55**, 1869–1887 (2013).
40. Blaauw, M. & Christen, J. A. Flexible paleoclimate age-depth models using an autoregressive gamma process. *Bayesian Anal.* **6**, 457–474 (2011).
41. Locarnini, R. A. et al. *World Ocean Atlas 2013. Volume 1, Temperature* (NOAA, 2013).
42. Wang, K. J. et al. Group 2 isochrysalides produce characteristic alkenones reflecting sea ice distribution. *Nat. Commun.* **12**, 15 (2021).
43. Sachs, J. P. Cooling of Northwest Atlantic slope waters during the Holocene. *Geophys. Res. Lett.* **34**, L03609 (2007).
44. Tierney, J. E., Haywood, A. M., Feng, R., Bhattacharya, T. & Otto-Bliesner, B. L. Pliocene warmth consistent with greenhouse gas forcing. *Geophys. Res. Lett.* **46**, 9136–9144 (2019).
45. Rayner, N. A. et al. Global analyses of sea surface temperature, sea ice, and night marine air temperature since the late nineteenth century. *J. Geophys. Res.* **108**, 4407 (2003).
46. Gray, W. R. & Evans, D. Nonthermal influences on Mg/Ca in planktonic foraminifera: a review of culture studies and application to the Last Glacial Maximum. *Paleoceanogr. Paleoclimatol.* **34**, 306–315 (2019).
47. Lambeck, K., Rouby, H., Purcell, A., Sun, Y. & Sambridge, M. Sea level and global ice volumes from the Last Glacial Maximum to the Holocene. *Proc. Natl. Acad. Sci. USA* **111**, 15296–15303 (2014).
48. Monnin, E. et al. Atmospheric CO₂ concentrations over the Last Glacial Termination. *Science* **291**, 112–114 (2001).
49. MacFarling Meure, C. et al. Law Dome CO₂, CH₄ and N₂O ice core records extended to 2000 years BP. *Geophys. Res. Lett.* **33**, L14810 (2006).
50. Rubino, M. et al. A revised 1000-year-old atmospheric ¹³C-CO₂ record from Law Dome and South Pole, Antarctica. *J. Geophys. Res. Atmos.* **118**, 8482–8499 (2013).
51. Marcott, S. A. et al. Centennial-scale changes in the global carbon cycle during the last deglaciation. *Nature* **514**, 616–619 (2014).
52. Ahn, J. & Brook, E. J. Siple Dome ice reveals two modes of millennial CO₂ change during the last ice age. *Nat. Commun.* **5**, 3723 (2014).
53. Bereiter, B. et al. Revision of the EPICA Dome C CO₂ record from 800 to 600 kyr before present. *Geophys. Res. Lett.* **42**, 542–549 (2015).
54. Olsen, A. et al. The Global Ocean Data Analysis Project version 2 (GLODAPv2) – an internally consistent data product for the world ocean. *Earth Syst. Sci. Data* **8**, 297–323 (2016).
55. Lisicki, L. E. & Raymo, M. E. A Pliocene-Pleistocene stack of 57 globally distributed benthic $\delta^{18}\text{O}$ records. *Paleoceanography* **20**, PA1003 (2005).
56. Schrag, D. P., Hampton, G. & Murray, D. W. Pore fluid constraints on the temperature and oxygen isotopic composition of the glacial ocean. *Science* **272**, 1930–1932 (1996).
57. LeGrande, A. N. & Schmidt, G. A. Global gridded data set of the oxygen isotopic composition in seawater. *Geophys. Res. Lett.* **33**, L12604 (2006).
58. Zhu, J., Poulsen, C. J. & Tierney, J. E. Simulation of Eocene extreme warmth and high climate sensitivity through cloud feedbacks. *Sci. Adv.* **5**, eaax1874 (2019).
59. Hurrell, J. W. et al. The community Earth system model: a framework for collaborative research. *Bull. Am. Meteorol. Soc.* **94**, 1339–1360 (2013).
60. Meehl, G. A. et al. Effects of model resolution, physics, and coupling on Southern Hemisphere storm tracks in CESM1.3. *Geophys. Res. Lett.* **46**, 12408–12416 (2019).
61. Zhu, J. et al. Reduced ENSO variability at the LGM revealed by an isotope-enabled Earth system model. *Geophys. Res. Lett.* **44**, 6984–6992 (2017).
62. Stevenson, S. et al. Volcanic eruption signatures in the isotope-enabled last millennium ensemble. *Paleoceanogr. Paleoclimatol.* **34**, 1534–1552 (2019).
63. Lüthi, D. et al. High-resolution carbon dioxide concentration record 650,000–800,000 years before present. *Nature* **453**, 379–382 (2008).
64. Loulergue, L. et al. Orbital and millennial-scale features of atmospheric CH₄ over the past 800,000 years. *Nature* **453**, 383–386 (2008).
65. Schilt, A. et al. Atmospheric nitrous oxide during the last 140,000 years. *Earth Planet. Sci. Lett.* **300**, 33–43 (2010).
66. Peltier, W. R., Argus, D. F. & Drummond, R. Space geodesy constrains ice age terminal deglaciation: The global ICE-6G_C (VM5a) model. *J. Geophys. Res. Solid Earth* **120**, 450–487 (2015).
67. DiNezio, P. N. et al. Glacial changes in tropical climate amplified by the Indian Ocean. *Sci. Adv.* **4**, eaat9658 (2018).
68. Duplessy, J. C., Labeyrie, L. & Waelbroeck, C. Constraints on the ocean oxygen isotopic enrichment between the Last Glacial Maximum and the Holocene: Paleoceanographic implications. *Quat. Sci. Rev.* **21**, 315–330 (2002).
69. Kageyama, M. et al. The PMIP4 contribution to CMIP6–part 4: scientific objectives and experimental design of the PMIP4-CMIP6 Last Glacial Maximum experiments and PMIP4 sensitivity experiments. *Geosci. Model Dev.* **10**, 4035–4055 (2017).
70. Otto-Bliesner, B. L. et al. The PMIP4 contribution to CMIP6–part 2: two interglacials, scientific objective and experimental design for Holocene and Last Interglacial simulations. *Geosci. Model Dev.* **10**, 3979–4003 (2017).
71. Lawrence, D. M. et al. Parameterization improvements and functional and structural advances in Version 4 of the Community Land Model. *J. Adv. Model. Earth Syst.* **3**, M03001 (2011).

72. Bartlein, P. J. & Shafer, S. L. Paleo calendar-effect adjustments in time-slice and transient climate model simulations (PaleoCalAdjust v1.0): impact and strategies for data analysis. *Geosci. Model Dev.* **12**, 3889–3913 (2019).
73. Whitaker, J. S. & Hamill, T. M. Ensemble data assimilation without perturbed observations. *Mon. Weather Rev.* **130**, 1913–1924 (2002).
74. Hamill, T. M. Interpretation of rank histograms for verifying ensemble forecasts. *Mon. Weather Rev.* **129**, 550–560 (2001).
75. Jones, T. R. et al. Water isotope diffusion in the WAIS Divide ice core during the Holocene and last glacial. *J. Geophys. Res. Earth Surface* **122**, 290–309 (2017).
76. Sokratov, S. A. & Golubev, V. N. Snow isotopic content change by sublimation. *J. Glaciol.* **55**, 823–828 (2009).
77. Comas-Bru, L. et al. Evaluating model outputs using integrated global speleothem records of climate change since the last glacial. *Clim. Past* **15**, 1557–1579 (2019).
78. Atsawaranunt, K. et al. The SISAL database: a global resource to document oxygen and carbon isotope records from speleothems. *Earth Syst. Sci. Data* **10**, 1687–1713 (2018).
79. Blunier, T. & Brook, E. J. Timing of millennial-scale climate change in Antarctica and Greenland during the Last Glacial Period. *Science* **291**, 109–112 (2001).
80. Stenni, B. et al. Expression of the bipolar see-saw in Antarctic climate records during the last deglaciation. *Nat. Geosci.* **4**, 46–49 (2011).
81. Watanabe, O. et al. Homogeneous climate variability across East Antarctica over the past three glacial cycles. *Nature* **422**, 509–512 (2003).
82. Brook, E. J. et al. Timing of millennial-scale climate change at Siple Dome, West Antarctica, during the last glacial period. *Quat. Sci. Rev.* **24**, 1333–1343 (2005).
83. Stenni, B. et al. The deuterium excess records of EPICA Dome C and Dronning Maud Land ice cores (East Antarctica). *Quat. Sci. Rev.* **29**, 146–159 (2010).
84. Steig, E. J. et al. Synchronous climate changes in Antarctica and the North Atlantic. *Science* **282**, 92–95 (1998).
85. Petit, J. R. et al. Climate and atmospheric history of the past 420,000 years from the Vostok ice core, Antarctica. *Nature* **399**, 429–436 (1999).
86. Markle, B. R. et al. Global atmospheric teleconnections during Dansgaard–Oeschger events. *Nat. Geosci.* **10**, 36–40 (2017).
87. Vinther, B. M. et al. Synchronizing ice cores from the Renland and Agassiz ice caps to the Greenland Ice Core Chronology. *J. Geophys. Res. Atmos.* **113**, D08115 (2008).
88. Stuiver, M. & Grootes, P. M. GISP2 oxygen isotope ratios. *Quat. Res.* **53**, 277–284 (2000).
89. Johnsen, S. J. et al. The $\delta^{18}\text{O}$ record along the Greenland Ice Core Project deep ice core and the problem of possible Eemian climatic instability. *J. Geophys. Res. Oceans* **102**, 26397–26410 (1997).
90. Andersen, K. K. et al. High-resolution record of Northern Hemisphere climate extending into the last interglacial period. *Nature* **431**, 147–151 (2004).
91. Holmgren, K. et al. Persistent millennial-scale climatic variability over the past 25,000 years in Southern Africa. *Quat. Sci. Rev.* **22**, 2311–2326 (2003).
92. Novello, V. F. et al. A high-resolution history of the South American Monsoon from Last Glacial Maximum to the Holocene. *Sci. Rep.* **7**, 44267 (2017).
93. Cheng, H. et al. The climate variability in northern Levant over the past 20,000 years. *Geophys. Res. Lett.* **42**, 8641–8650 (2015).
94. Dutt, S. et al. Abrupt changes in Indian summer monsoon strength during 33,800 to 5500 years B.P. *Geophys. Res. Lett.* **42**, 5526–5532 (2015).
95. Ayliffe, L. K. et al. Rapid interhemispheric climate links via the Australasian monsoon during the last deglaciation. *Nat. Commun.* **4**, 2908 (2013).
96. Partin, J. W., Cobb, K. M., Adkins, J. F., Clark, B. & Fernandez, D. P. Millennial-scale trends in west Pacific warm pool hydrology since the Last Glacial Maximum. *Nature* **449**, 452–455 (2007).
97. Cai, Y. et al. Variability of stalagmite-inferred Indian monsoon precipitation over the past 252,000 y. *Proc. Natl Acad. Sci. USA* **112**, 2954–2959 (2015).
98. Fleitmann, D. et al. Timing and climatic impact of Greenland interstadials recorded in stalagmites from northern Turkey. *Geophys. Res. Lett.* **36**, L19707 (2009).
99. Cruz, F. W. et al. Insolation-driven changes in atmospheric circulation over the past 116,000 years in subtropical Brazil. *Nature* **434**, 63–66 (2005).
100. Hellstrom, J., McCulloch, M. & Stone, J. A detailed 31,000-year record of climate and vegetation change, from the isotope geochemistry of two New Zealand speleothems. *Quat. Res.* **50**, 167–178 (1998).
101. Grant, K. M. et al. Rapid coupling between ice volume and polar temperature over the past 150,000 years. *Nature* **491**, 744–747 (2012).
102. Cheng, H. et al. Climate change patterns in Amazonia and biodiversity. *Nat. Commun.* **4**, 1411 (2013).

Acknowledgements We thank B. Malevich for early discussions and explorations on LGM-to-present data assimilation, and M. Fox and N. Rapp for help in compiling the proxy data. We thank P. DiNezio for providing initial and boundary condition files for the CESM simulations, and B. Markle for assistance in compiling and sharing the ice core water isotope data. This study was supported by National Science Foundation (NSF) grant numbers AGS-1602301 and AGS-1602223, and Heising-Simons Foundation grant numbers 2016-012, 2016-014 and 2016-015. The CESM project is supported primarily by the NSF. This material is based on work supported by the National Center for Atmospheric Research, which is a major facility sponsored by the NSF under Cooperative Agreement No. 1852977. Computing and data storage resources, including the Cheyenne supercomputer (<https://doi.org/10.5065/D6RX99H4>), were provided by the Computational and Information Systems Laboratory (CISL) at NCAR.

Author contributions M.B.O. conducted the data assimilation, led the analysis and interpretation of the results, and designed the figures. M.B.O. and J.E.T. led the writing of this paper. J.E.T. led the proxy data compilation. J.K. wrote the DASH code, based on methods and input by R.T. and G.J.H. J.Z. and C.J.P. planned and conducted the iCESM simulations. All authors contributed to the design of the study and the writing of this manuscript.

Competing interests The authors declare no competing interests.

Additional information

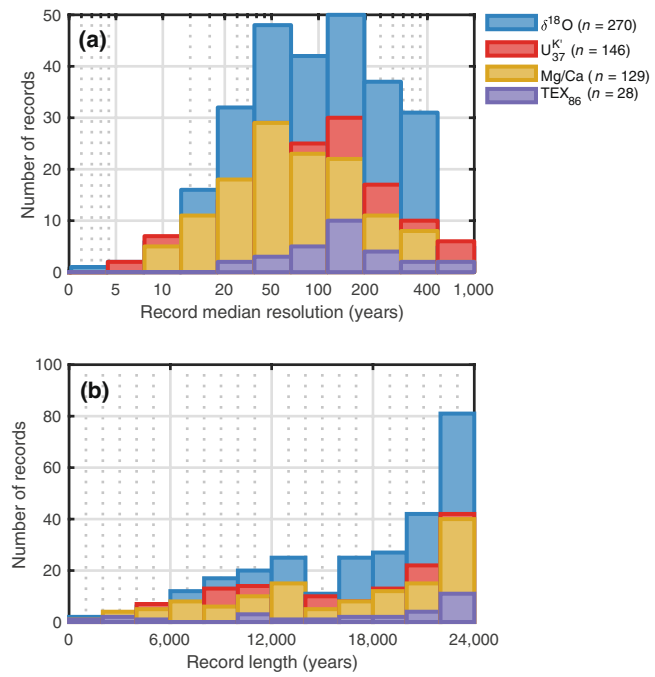
Supplementary information The online version contains supplementary material available at <https://doi.org/10.1038/s41586-021-03984-4>.

Correspondence and requests for materials should be addressed to Matthew B. Osman.

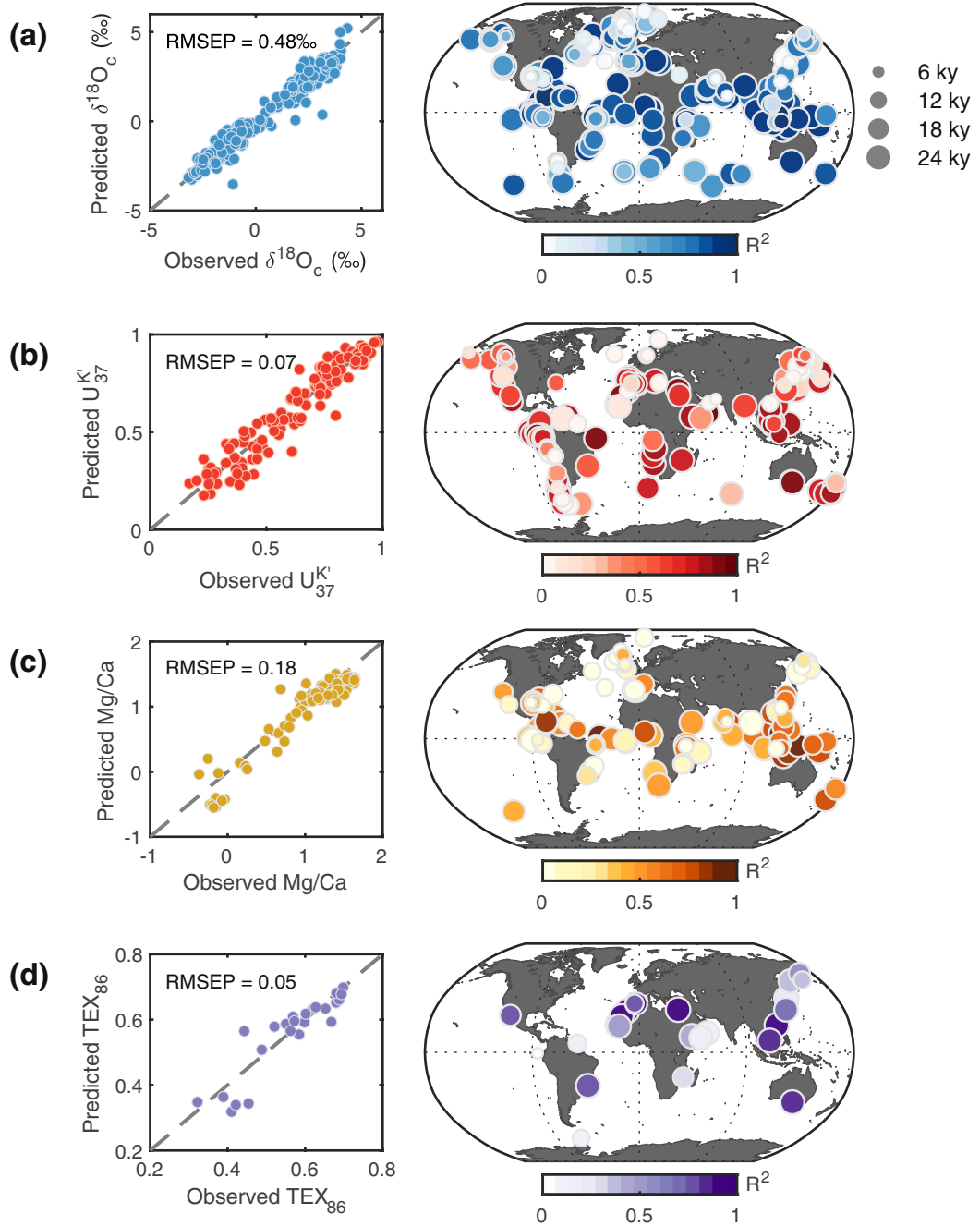
Peer review information *Nature* thanks William Gray and the other, anonymous, reviewer(s) for their contribution to the peer review of this work. Peer reviewer reports are available.

Reprints and permissions information is available at <http://www.nature.com/reprints>.

Article



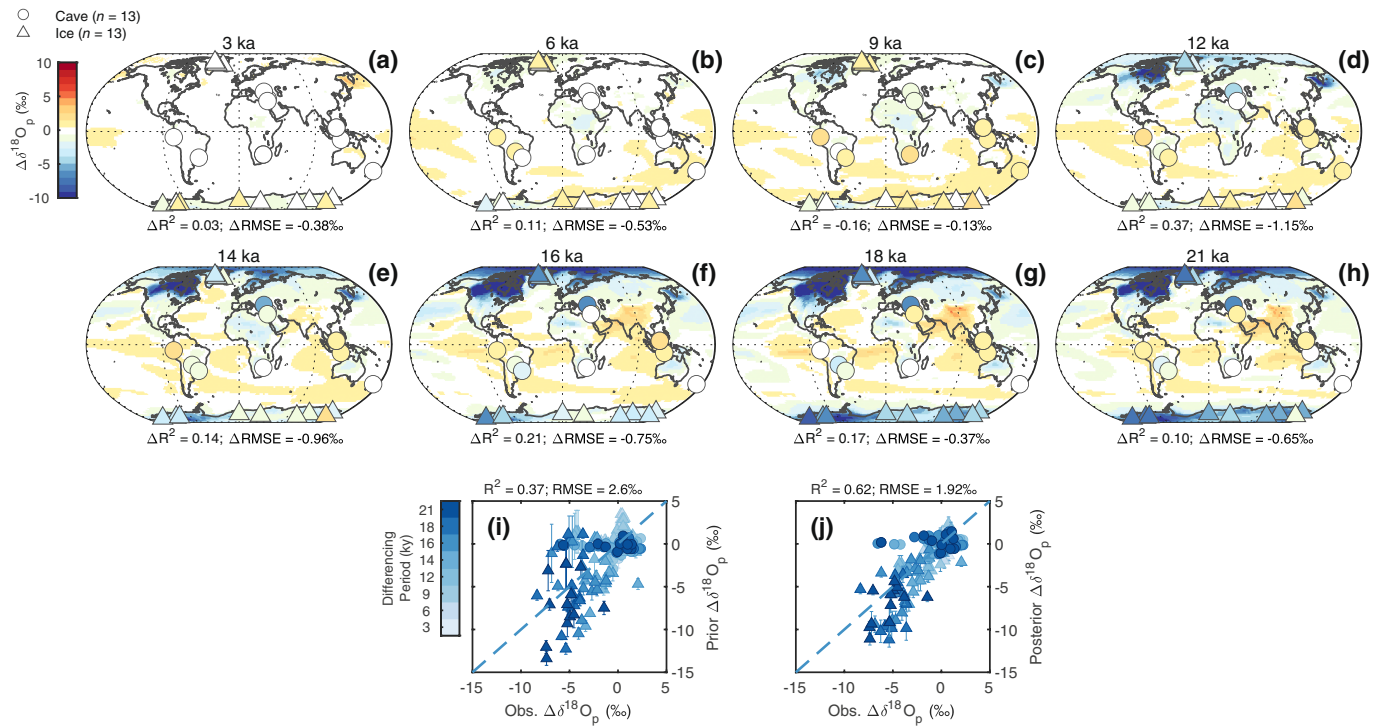
Extended Data Fig. 1 | Time resolution and temporal coverage of the SST proxy data compilation. **a**, Histogram of record resolution (denoting the median sample resolution for each record), computed for each proxy type. **b**, Histogram of record length for each proxy type.



Extended Data Fig. 2 | Statistical validation of randomly withheld marine geochemical proxies. **a**, From left: observed versus forward-modelled $\delta^{18}\text{O}_c$ mean values for each site using the posterior data assimilation estimates. Shown at right are the associated median $R^2_{\text{validation}}$ scores (each based on

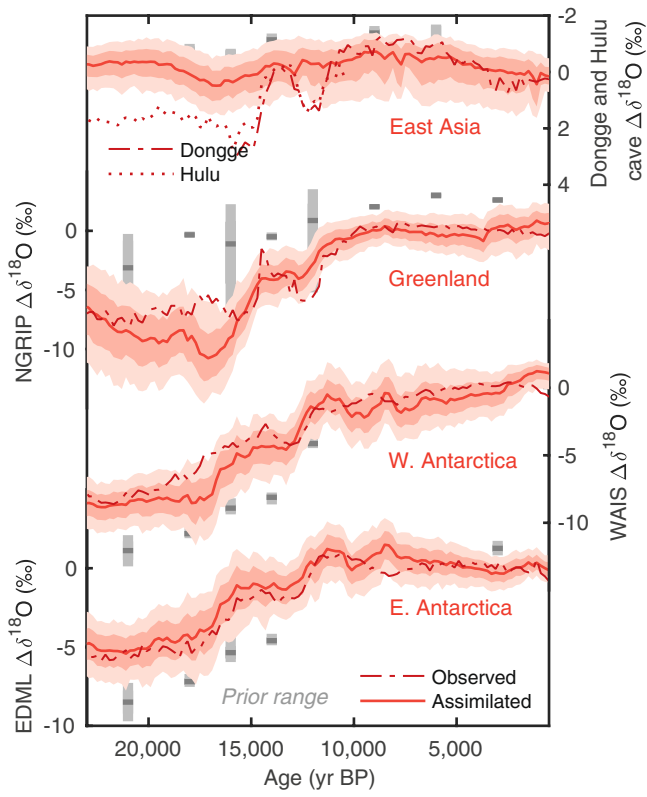
$n = 100$ LGMR ensemble members), computed on a per-site basis (see Methods section “Internal and external validation testing”). **b–d**, As in **a**, but for U_{37}^K (**b**), Mg/Ca (**c**) and TEX_{86} (**d**), respectively.

Article



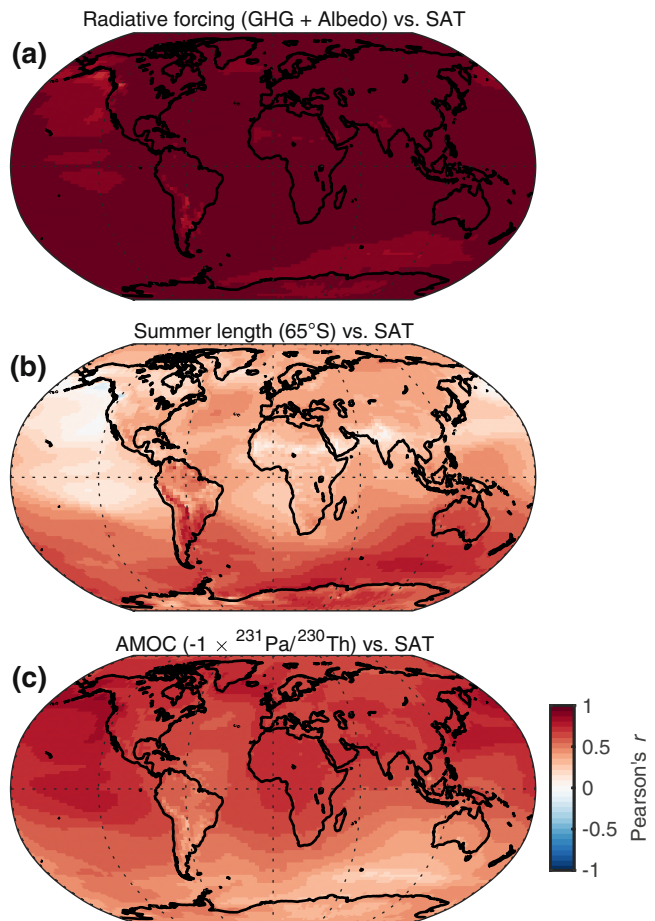
Extended Data Fig. 3 | Validation using independent $\delta^{18}\text{O}_p$ ice core and speleothem records. **a**, 3 ka–preindustrial (PI; 0 ka) posterior $\Delta\delta^{18}\text{O}_p$ field; overlying markers show the observed 3 ka–PI $\Delta\delta^{18}\text{O}_p$ values from speleothems and ice cores. Only records spanning at least 18 of the past 24 kyr are shown. ΔR^2 and ΔRMSEP values denote the change in observed versus posterior assimilated $\Delta\delta^{18}\text{O}_p$ values relative to the prior (that is, iCESM) estimated values.

b–h, As in **a**, but for values differenced at 6, 9, 12, 14, 16, 18 and 21 ka versus the PI, respectively. **i**, All observed $\Delta\delta^{18}\text{O}_p$ versus model prior values; dashed line indicates the 1:1 relationship. **j**, All observed $\Delta\delta^{18}\text{O}_p$ versus posterior values, which show a strong improvement in ΔR^2 and ΔRMSEP over the prior. Note that each scatter point shown in panels **i,j** corresponds to an external validation site shown in panels **a–h**.

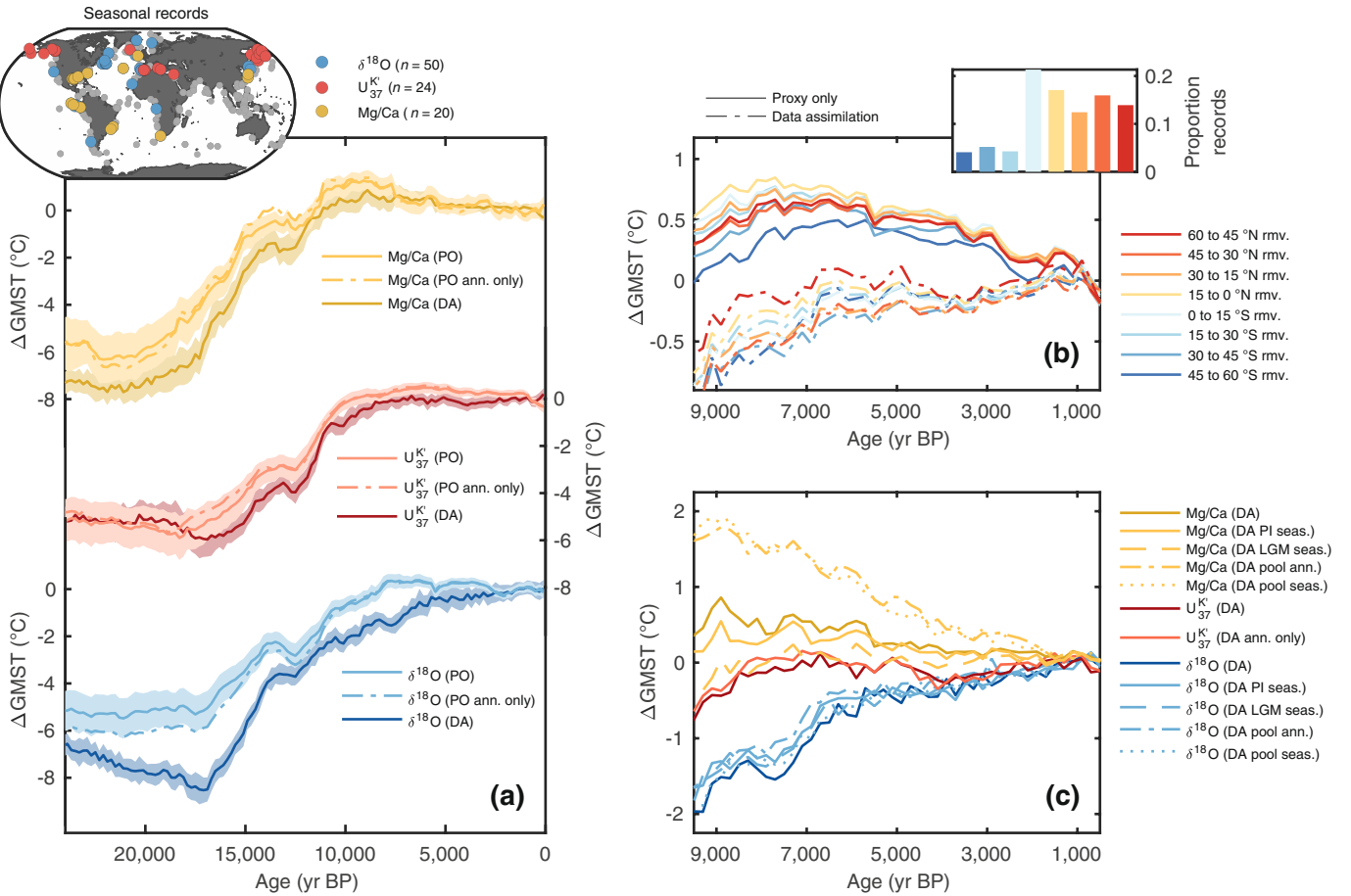


Extended Data Fig. 4 | Time-comparison of posterior LGMR $\delta^{18}\text{O}_p$ with selected $\delta^{18}\text{O}_p$ ice core and speleothem records. Uncertainty ranges denote the $\pm 1\sigma$ level (dark) and 95% confidence range (light) from the LGMR ensemble. Also shown for comparison are the full range (shaded grey) and median iCESM time slice prior values (50-year means) for each site. See also Extended Data Table 2.

Article

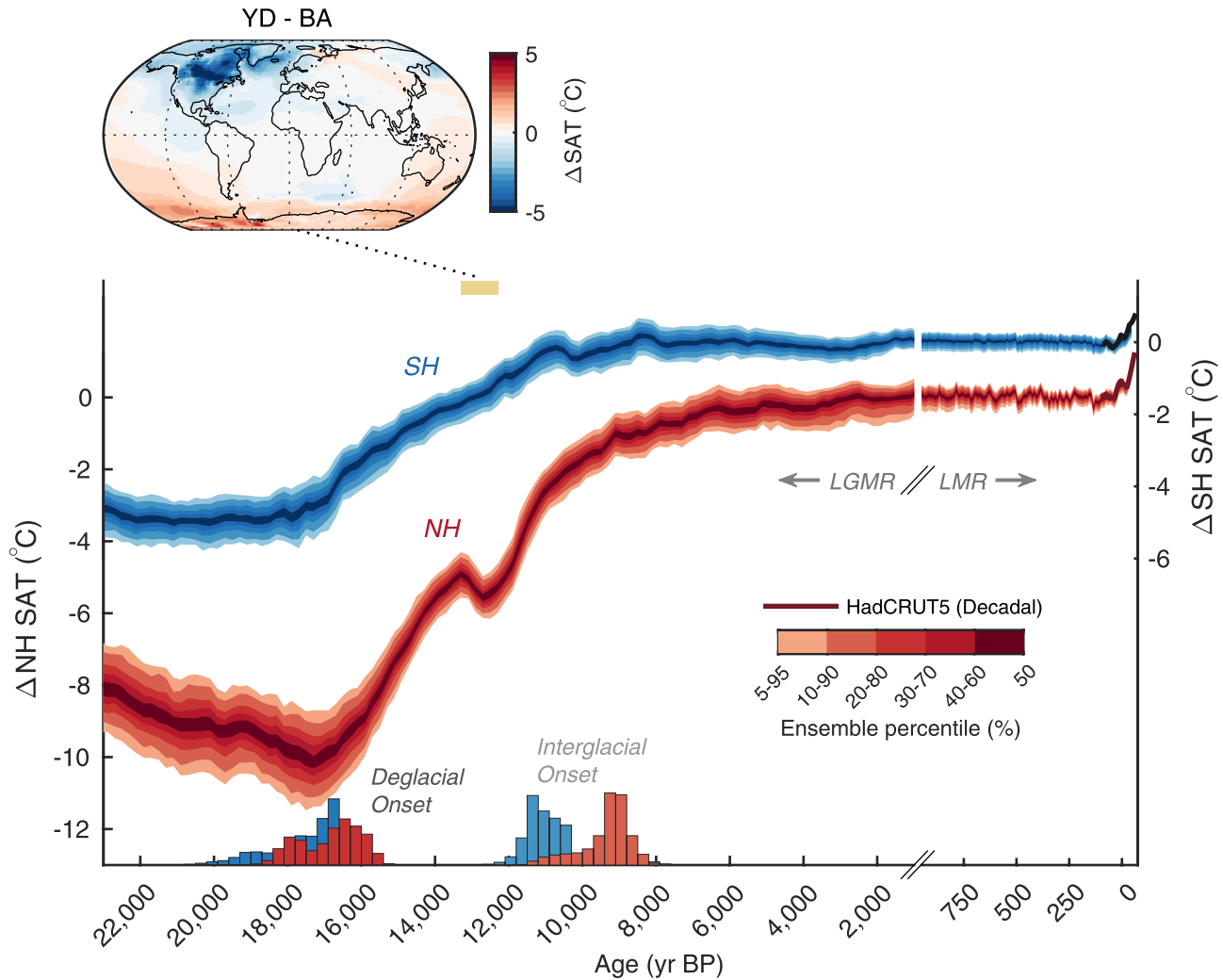


Extended Data Fig. 5 | Influences on global surface temperature evolution during the past 24 kyr. a–c, Spatial LGM-to-present correlations between surface air temperature (SAT) and combined greenhouse gas²⁴ and global albedo radiative forcing¹³ (a); summer length at 65°S,²⁷ (b); and the $-1 \times {}^{231}\text{Pa}/{}^{230}\text{Th}$ AMOC proxy index from Bermuda Rise^{29–31} (c; shown such that SAT correlations are positive with AMOC strength).



Extended Data Fig. 6 | Proxy-specific GMST reconstructions and comparison of Holocene GMST trends. **a.** $\delta^{18}\text{O}$, U_{37}^K , and Mg/Ca-derived GMST reconstructions, derived using both the proxy-only (PO) and data assimilation (DA) approaches. In a, the shaded regions show the $\pm 1\sigma$ range across $n = 50$ ensemble members for the DA-based GMST estimates, and $n = 10,000$ realizations for the PO-based GMST estimates (note uncertainty ranges are not shown for the dotted-dashed curves). **b.** Sensitivity of the Holocene GMST evolution to the removal of proxies situated in contiguous 15° latitudinal bands,

both for the PO and DA approaches. **c.** Sensitivity of the DA-based Holocene GMST evolution to proxy seasonality (computed by fixing foraminifera growth seasonality to either preindustrial (PI) or LGM monthly SSTs for Mg/Ca and $\delta^{18}\text{O}$, or by removing records with seasonal alkenone production for U_{37}^K), and to the ‘pooled’ foraminifera species SST calibrations of refs.^{20,21} (see Supplementary Information). All ΔGMST time series denote deviations relative to the past 2 kyr.


Extended Data Fig. 7 | Hemispheric variability during the past 24 kyr.

Ensemble distribution ($n=500$) of LGMR-estimated Northern Hemisphere (NH; red) and Southern Hemisphere (SH; blue) mean hemispheric temperatures during the past 24 kyr. Shown at top is the surface temperature spatial difference for the Bølling–Allerød (BA) and Younger Dryas (YD) intervals.

Range of hemispheric last deglacial and interglacial onset timings are shown as histograms at bottom. The LGMR is plotted alongside reconstructed decadal hemispheric temperatures from the last millennium reanalysis v2.1¹⁷ and HadCRUT5 observational product¹¹.

Extended Data Table 1 | Information on the iCESM simulations used for generating model priors

Age (ka)	Model description	Number of priors	Greenhouse gas (CO ₂ /CH ₄ /N ₂ O)	Global δ ¹⁸ O _{sw}	GMST range (°C)	Citation
0	iCESM1.2: PI	16	285 / 792 / 276	0.05	14.03–14.25	10
0	iCESM1.2: PI	10	285 / 792 / 276	0.05	13.22–13.33	61
0	iCESM1.3: PI	10	285 / 792 / 276	0.05	13.68–13.84	61
0	iCESM1.2 Last Millennium Member #2: 850–1850 CE	20	Transient	0.05	12.96–13.26	62
0	iCESM1.2 Last Millennium Member #3: 850–1850 CE	20	Transient	0.05	12.98–13.27	62
3	iCESM1.2: 3 ka	16	275 / 580 / 270	0.05	13.99–14.14	10
6	iCESM1.2: 6 ka w/ Sahara & 50–90°N greened	16	264 / 597 / 262	0.05	14.14–14.62	This study
6	iCESM1.2: 6 ka	8	264 / 597 / 262	0.05	14.03–14.19	This study
9	iCESM1.2: 9 ka w/ Sahara greened	16	260 / 659 / 255	0.34	13.87–14.09	This study
12	iCESM1.2: 12 ka	16	253 / 478 / 236	0.59	12.61–12.76	This study
12	iCESM1.2: 12 ka w/ freshwater over N. Atl.	4	253 / 478 / 236	0.59	10.79–11.77	This study
14	iCESM1.2: 14 ka	16	238 / 637 / 255	0.73	10.05–10.32	This study
16	iCESM1.2: 16 ka	16	224 / 452 / 199	0.90	9.27–9.45	This study
16	iCESM1.2: 16 ka w/ freshwater over N. Atl.	4	224 / 452 / 199	0.90	7.63–8.45	This study
18	iCESM1.2: 18 ka	16	190 / 370 / 245	1.02	8.00–8.13	10
21	iCESM1.2: 21 ka	16	190 / 375 / 200	1.05	7.41–7.87	10
21	iCESM1.3: 21 ka	18	190 / 375 / 200	1.05	6.40–7.37	61

Greenhouse gas concentrations are in ppm for CO₂ and ppb for CH₄ and N₂O. Global mean seawater δ¹⁸O (δ¹⁸O_{sw}) is in ‰ relative to the Vienna Standard Mean Ocean Water (VSMOW). See Methods for details of the implementation of vegetation and freshwater forcing in related simulations.

Article

Extended Data Table 2 | Geographical and site identification information for ice core and speleothem $\delta^{18}\text{O}_\text{p}$ records used for LGMR external validation

Proxy class	Site name	Lat. ($^{\circ}\text{N}$)	Lon. ($^{\circ}\text{E}$)	R ²	CE	Citation
Ice core	Byrd	-80.02	-119.53	0.82	-0.71	79
Ice core	EDC	-75.10	123.35	0.89	0.49	80
Ice core	EDML	-75.00	0.07	0.86	0.78	80
Ice core	Fuji	-77.32	38.70	0.83	0.66	81
Ice core	Siple	-81.65	-149.00	0.88	0.64	82
Ice core	TALDICE	-72.82	159.18	0.89	0.76	83
Ice core	Taylor	-77.78	158.72	0.65	-0.65	84
Ice core	Vostok	-78.46	106.84	0.88	0.85	85
Ice core	WAIS	-79.47	-112.00	0.87	0.22	86
Ice core	Renland	71.27	-26.73	0.74	0.20	87
Ice core	GISP2	72.60	-38.50	0.65	0.05	88
Ice core	GRIP	72.58	-37.63	0.58	-0.21	89
Ice core	NGRIP	75.10	-42.33	0.71	0.55	90
Speleothem	Cold Air cave	-24.00	29.18	0.08	-14.58	91
Speleothem	Jaraguá cave	-21.08	-56.58	0.27	-1.63	92
Speleothem	Jeita cave	33.95	35.65	0.01	-15.69	93
Speleothem	Mawmluh cave	25.26	91.88	0.42	-4.47	94
Speleothem	Liang Luar cave	-8.53	120.43	0.06	-5.19	95
Speleothem	Bukit Assam cave	4.03	114.80	0.04	-5.23	96
Speleothem	Xiaobailong cave	24.20	103.36	0.20	-3.55	97
Speleothem	Sofular cave	41.42	31.93	0.04	-1.86	98
Speleothem	Botuverá	-27.22	-49.16	0.10	-7.88	99
Speleothem	Gunung-buda cave	4.03	114.80	0.02	-2.66	96
Speleothem	Nettlebed cave	-41.25	172.63	0.27	-4.11	100
Speleothem	Soreq cave	31.76	35.02	0.17	-5.45	101
Speleothem	El Condor cave	-5.93	-77.30	0.02	-0.42	102

Data from refs. 79–102.

Extended Data Table 3 | External validation statistics associated with different choices of covariance localization and the 1 σ ‘length-scale’ range of the evolving prior sampling

Localization (km) :	6,000	9,000	12,000	15,000	18,000	21,000	24,000	∞
ΔR^2	0.09	0.19	0.23	0.24	0.24	0.25	0.25	0.16
$\Delta RMSEP$ (%)	-0.54	-0.59	-0.63	-0.63	-0.64	-0.72	-0.73	-0.34
Length scale (yr) :	2,000	3,000	4,000	5,000	6,000	∞		
$\Delta \bar{R}^2$	0.23	0.24	0.25	0.24	0.23	0.18		
$\Delta \bar{RMSEP}$ (%)	-0.63	-0.62	-0.64	-0.65	-0.69	-0.58		

ΔR^2 and $\Delta RMSEP$ values denote the change in observed versus posterior assimilated $\Delta\delta^{18}\text{Op}$ values relative to the prior iCESM estimated values; larger ΔR^2 and smaller $\Delta RMSEP$ thus denote greater improvement in the assimilated posterior relative to iCESM (see Extended Data Fig. 2i, j for plotted LGMR values). For localization testing, listed ΔR^2 and $\Delta RMSEP$ values represent the median across all ($n=6$) length-scale tests; for length-scale testing, listed $\Delta \bar{R}^2$ and $\Delta \bar{RMSEP}$ values represent the median across all ($n=8$) localization tests.